IOWA STATE UNIVERSITY
Digital Repository

Retrospective Theses and Dissertations

Iowa State University Capstones, Theses and Dissertations

1985

Optical properties of dilute Ag(Ni) alloys

James L. Wolf
Iowa State University

Follow this and additional works at: https://lib.dr.iastate.edu/rtd

 Part of the Condensed Matter Physics Commons

Recommended Citation
Wolf, James L., "Optical properties of dilute Ag(Ni) alloys " (1985). *Retrospective Theses and Dissertations*. 12120.
https://lib.dr.iastate.edu/rtd/12120

This Dissertation is brought to you for free and open access by the Iowa State University Capstones, Theses and Dissertations at Iowa State University Digital Repository. It has been accepted for inclusion in Retrospective Theses and Dissertations by an authorized administrator of Iowa State University Digital Repository. For more information, please contact digirep@iastate.edu.

www.manaraa.com

INFORMATION TO USERS

This reproduction was made from a copy of a document sent to us for microfilming. While the most advanced technology has been used to photograph and reproduce this document, the quality of the reproduction is heavily dependent upon the quality of the material submitted.

The following explanation of techniques is provided to help clarify markings or notations which may appear on this reproduction.

1. The sign or "target" for pages apparently lacking from the document photographed is "Missing Page(s)". If it was possible to obtain the missing page(s) or section, they are spliced into the film along with adjacent pages. This may have necessitated cutting through an image and duplicating adjacent pages to assure complete continuity.

2. When an image on the film is obliterated with a round black mark, it is an indication of either blurred copy because of movement during exposure, duplicate copy, or copyrighted materials that should not have been filmed. For blurred pages, a good image of the page can be found in the adjacent frame. If copyrighted materials were deleted, a target note will appear listing the pages in the adjacent frame.

3. When a map, drawing or chart, etc., is part of the material being photographed, a definite method of "sectioning" the material has been followed. It is customary to begin filming at the upper left hand corner of a large sheet and to continue from left to right in equal sections with small overlaps. If necessary, sectioning is continued again–beginning below the first row and continuing on until complete.

4. For illustrations that cannot be satisfactorily reproduced by xerographic means, photographic prints can be purchased at additional cost and inserted into your xerographic copy. These prints are available upon request from the Dissertations Customer Services Department.

5. Some pages in any document may have indistinct print. In all cases the best available copy has been filmed.

University Microfilms International
300 N. Zeeb Road
Ann Arbor, MI 48106

8524710

Wolf, James L.

OPTICAL PROPERTIES OF DILUTE SILVER(NICKEL) ALLOYS

Iowa State University PH.D. 1985

University
Microfilms
International 300 N. Zeeb Road, Ann Arbor, MI 48106

Optical properties of dilute Ag(Ni) alloys

by

James L. Wolf

A Dissertation Submitted to the
Graduate Faculty in Partial Fulfillment of the
Requirements for the Degree of
DOCTOR OF PHILOSOPHY

Department: Professional Studies in Education
Major: Education (Higher Education)

Approved:

Members of the Committee:

Signature was redacted for privacy.

Signature was redacted for privacy.

In Charge of Major Work

Signature was redacted for privacy.

For the Major Department

Signature was redacted for privacy.

For the Graduate College

Iowa State University
Ames, Iowa

1985

TABLE OF CONTENTS

ACKNOWLEDGEMENTS

The path to completion of this dissertation has been overly long and marked by periods of intense activity separated by long periods of inactivity. The personal satisfaction of finally completing my degree program will remove the lurking dissatisfaction with myself that has been present for all too many years.

My wife, Judy, and our children have suffered patiently through the activity and inactivity periods. They have remained supportive and loving throughout. Their support has been irreplaceable. Their love is cherished.

Special thanks are due Dr. David Lynch, who never shut the door, and Dr. Anton Netusil, whose prodding, encouragement and handling local arrangements in Ames led to the final push over the procedural hurdles to completion.

Many others deserve mention here, mostly for their gentle or not so gentle prodding. From the Cedar Falls contingent of this group, Dr. Marlene Strathe deserves explicit mention for pushing me to swallow my pride and make the final push. From the Ames contingent, Dr. Daniel Zaffarano deserves mention for making me feel guilty every time I saw him. His smile brought me to Ames. I'll enjoy it again at graduation.

NOTATION

Throughout this dissertation, vector quantities are emboldened. For example, the electric field strength vector, E, is consistently presented as **E**.

Complex quantities are indicated by a tilde (~) placed over the quantity. For example, the complex dielectric function is represented as $\tilde{\varepsilon}$.

THEORY AND REVIEW OF RELATED RESEARCH

The study of the optical properties of dilute Ag(Ni) alloys begins with a development of the theory of the interaction of electromagnetic radiation with solids, particularly metals. Emphasis is placed on those aspects of the theory which lead to quantities measured in this study and on the role of the dielectric function, $\tilde{\varepsilon}(\omega)$. Models of electronic properties of metallic alloys are then discussed, leading to a presentation of the virtual bound state model which has been successfully applied in systems similar to the Ag(Ni) system. Finally, experimental research on the optical properties of dilute alloys of transition metals in noble metals is reviewed.

Interaction of light with metals

The interaction of electromagnetic radiation in the infrared and visible regions with solids is described macroscopically by Maxwell's equations. For isotropic media with permeability, μ, equal to unity, these equations can be written as:

$$\begin{aligned} \nabla \times \mathbf{B} &= \frac{1}{c}\frac{\partial \mathbf{D}}{\partial t} + \frac{4\pi}{c}\mathbf{J} \\ \nabla \times \mathbf{E} &= -\frac{1}{c}\frac{\partial \mathbf{B}}{\partial t} \\ \nabla \cdot \mathbf{B} &= \nabla \cdot \mathbf{D} = 0 \end{aligned} \tag{1}$$

where the constitutive equations which contain information about the medium in which the electric and magnetic fields propagate are:

$$\begin{aligned} \mathbf{J} &= \sigma\mathbf{E} \\ \mathbf{D} &= \varepsilon\mathbf{E} \\ \mathbf{B} &= \mathbf{H} \end{aligned} \tag{2}$$

In the case of electromagnetic radiation the fields depend on time as

$$\tilde{E}(t) = \tilde{E}_0 e^{-i\omega t} \tag{3}$$

The first of Maxwell's equations can then be written

$$\nabla \times B = \frac{1}{c} \tilde{\varepsilon} \frac{\partial E}{\partial t} \tag{4}$$

where $\tilde{\varepsilon}$ is the complex dielectric constant,

$$\tilde{\varepsilon} = \varepsilon + i \frac{4\pi}{\omega} \sigma = \varepsilon_1 + i\varepsilon_2 \tag{5}$$

It is through this quantity that theoretical models of materials make contact with physically observable quantities.

If we assume that the radiation is represented as a plane wave, the electric field can be written

$$\tilde{E}(r,t) = \tilde{E}_0 e^{i(\tilde{q}\cdot r - \omega t)} \tag{6}$$

where

$$\begin{aligned} \tilde{E}_0 &= E_{01} + iE_{02} \\ \tilde{q} &= q_1 + iq_2 \end{aligned} \tag{7}$$

Here $\tilde{q}$ is the complex wave vector of propagation in the medium. The wave equation then becomes

$$\nabla^2 \tilde{E} = \frac{1}{c^2} \varepsilon \frac{\partial^2 \tilde{E}}{\partial t^2} + 4\pi\sigma \frac{\partial \tilde{E}}{\partial t} \tag{8}$$

Substituting Equation (6) and cancelling common factors we obtain

$$\tilde{q}\cdot\tilde{q} = \frac{\omega^2}{c^2} \left[\varepsilon + i \frac{4\pi\sigma}{\omega} \right] = \frac{\omega^2}{c^2} \tilde{\varepsilon} \tag{9}$$

This implies that the magnitude of the complex propagation vector is related to the dielectric constant of the medium

$$|\tilde{q}| = \frac{\omega}{c} |\sqrt{\tilde{\varepsilon}}| \tag{10}$$

As a result, the fields within the medium will have the form

$$\tilde{E}(r,t) = \tilde{E}_0 e^{i(\frac{\omega}{c} |\sqrt{\tilde{\varepsilon}}| \hat{q}\cdot r - \omega t)} \tag{11}$$

The index of refraction is defined (for the special case of $\mathbf{q} \parallel \mathbf{r}$) as the ratio of the phase velocity of the wave in a vacuum, c, to that in the medium.

$$n = \frac{c}{v} = \frac{cq}{\omega} \tag{12}$$

This leads us to define, by analogy, a complex index of refraction

$$\tilde{N} = \frac{c}{\omega}\tilde{q} = \tilde{\varepsilon} = n + ik \tag{13}$$

Substituting this expression into Equation (11) leads to a more physically understandable result

$$\begin{aligned} E(r,t) &= E_0 e^{i[\frac{\omega}{c}(n + ik)\hat{q}\cdot r - \omega t]} \\ &= E_0 e^{-\frac{\omega k}{c}\hat{q}\cdot r} e^{i[\frac{\omega}{c}n\hat{q}\cdot r - \omega t]} \end{aligned} \tag{14}$$

The first exponential term shows that the plane wave will be damped for $k > 0$. Because of this observation, k is sometimes referred to as the extinction coefficient. The concept of an optical skin depth flows directly from this expression.

From a theoretical point of view, it is more convenient to derive the complex dielectric constant, $\tilde{\varepsilon}(\omega)$, of a metal than it is to compute $\tilde{N}(\omega)$ directly. Using the random phase approximation (RPA) to describe the effect of induced fields in the medium, Ehrenreich and Cohen [1] have shown that

$$\varepsilon_{RPA} = 1 - \frac{\omega_p^2}{\omega(\omega+i/\tau_c)} - \frac{e^2}{m\pi^2}\sum_{i,f}\int d^3q \frac{f_{if}(q)}{(\omega+i/\tau_{if})^2-(\omega_f(q)-\omega_i(q))^2} \tag{15}$$

Here i and f refer to the initial and final states of the electron excited by the electromagnetic wave. The oscillator strength

$$f_{if}(q) = \frac{2|\hat{e}\cdot p_{if}|^2}{mh\omega(q)} \tag{16}$$

describes the transition rate between two particular electronic states i and f, $\hat{e}$ is the electric unit vector and p_{if} is dipole matrix element

$$p_{if} = \langle i|p|f\rangle = \langle q + g|p|q\rangle \tag{17}$$

The plasma frequency, ω_p, in the second term is defined by

$$\omega_p^2 = \frac{4\pi Ne^2}{m^*_{opt}} \tag{18}$$

The first two items in Equation (16) give rise to the Drude or intraband contribution to the dielectric function, while the third term represents the interband contribution. Thus, the dielectric constant can be separated into components

$$\tilde{\varepsilon}_{total} = \tilde{\varepsilon}_{intraband} + \tilde{\varepsilon}_{interband} \tag{19}$$

The intraband contribution represents the response of the free electron gas to the electromagnetic field. The plasma frequency is the resonant frequency for longitudinal motion of the electron gas. In a real crystal at a finite temperature electrons scatter off phonons, making momentum conserving transitions between states in the same band possible. In this model for $\tilde{\varepsilon}_{intraband}$, the electron-phonon scattering is phenomenologically accounted for through τ_c, the relaxation time. It is interesting to note that the presence of other scattering events besides electron-phonon events could be included in this model by speaking of an effective relaxation time, τ_{eff}, such that

$$\frac{1}{\tau_{eff}} = \frac{1}{\tau_c} + \frac{1}{\tau_1} + \frac{1}{\tau_2} + \ldots + \frac{1}{\tau_n} \tag{20}$$

where the τ_n are relaxation times for the other scattering mechanisms. Thus, point imperfections, such as vacancies or substitutional impurities, can be accommodated. Even when the density of conduction electrons and the shape of the Fermi surface are changed, the model can be made to fit the observed dielectric constant by electing to use an effective optical mass.

The interband portion of the dielectric function represents the case where electrons make transitions to other states characterized by the same q in the reduced zone scheme. The relaxation time, τ_{if}, results from the finite lifetime of the final state. Its effect is to broaden the observed absorption. If the dipole matrix elements are assumed to be constant over all of q-space, $\varepsilon_{2\ \text{interband}}$ can be written in terms of a quantity known as the joint density of states (JDOS)

$$\varepsilon_{2\ \text{interband}} \propto \text{JDOS} = \frac{1}{\omega^2}\int d^3q\ \delta(E_i-E_f-h\omega)f(E_i)[1-f(E_f)] \quad (21)$$

The JDOS represents the probability of finding a pair of energy states characterized by the same q separated by hω. While the assumption of constant p_{if} is clearly not appropriate in general, structure in the observed ε_2 can often be related to the calculated band structure through comparison of ε_2 with the JDOS.

In non-crystalline solids or disordered solids the expression for $\varepsilon_{2\ \text{interband}}$ is no longer valid since q may no longer be an adequate quantum number. As a result, it is not clear that it is appropriate to speak of a conventional band structure. Calculations of ε_2 based on the band structure can no longer be made. The joint density of states

concept may retain its validity even in this situation, however, if the computational dependence on $\mathbf{q}$ can be eliminated.

The preceding development shows the importance of the measurement of the optical properties of solids. Because the dielectric function is readily calculated from models of electronic states in solids, optical properties provide a relatively direct point of comparison between experiment and theory. Optical properties also have the advantage of providing information about electronic states with an energy range $E_F - h\omega \leq E \leq E_F + h\omega$, where E_F is the Fermi energy and $h\omega$ is the energy of the incident photon. Direct comparison between optical properties and band structure calculations is rarely easy, however. Band calculation results are displayed for symmetry directions only. However, because the JDOS at a particular energy contains contributions from all of $\mathbf{q}$-space, it provides an especially useful way of displaying band structure results for comparison with optical data.

Reflectivity and absorptivity

While calculations discussed above most often involve quantities characteristic of the electronic states within the solid, measurements of optical properties of solids usually involve observation of propagational characteristics of light within the solid or at the boundary between the solid and a medium having different optical characteristics. The formulation of optical properties in terms of the complex index of refraction, $\tilde{N}$, leads more directly to observable quantities. As we have seen earlier, the two formulations are related through Equation (13).

The measurable quantity of interest in this study is the absorptivity of the solid. Experimentally, a light beam traveling in vacuum arrives at the surface of a solid. The propagational characteristics of light in the solid are different than in vacuum. The energy carried in the incident beam is split into a reflected component and a transmitted component. Application of the boundary conditions yields an expression for the reflectance wave amplitude for normal incidence,

$$\tilde{r} = \tilde{E}_r/\tilde{E}_i = (1 - \tilde{N})/(1 + \tilde{N}) \tag{22}$$

where the subscripts r and i identify the reflected and incident waves. Reflectivity is defined as

$$R = \tilde{r}^*\tilde{r} = |(1 - \tilde{N})/(1 + \tilde{N})|^2 \tag{23}$$

This quantity is equivalent to the fraction of the power carried in the reflected wave.

At the boundary the quantity that is complementary to reflectivity is transmissivity, the fraction of the power carried in the wave transmitted through the boundary. In an opaque sample, all of the energy transmitted through the boundary is eventually absorbed in the medium. The transmissivity then is equal to the absorptivity, the fraction of the power absorbed in the new medium. This leads to the conveniently simple result,

$$A = 1 - R \tag{24}$$

where A is the absorptivity.

It is apparent that frequency dependent changes in ε will result in corresponding changes in reflectivity and absorptivity. It is also

apparent that the relationship between A and ε is not a simple linear one.

The optical properties of silver

Silver serves as a convenient example of the utility of the decomposition of ε into intraband and interband components. Figure 1 shows Ehrenreich and Philipp's [2] calculation of ε_1 and its decomposition into components. Their methodology involves identification of the Drude-like region by examination of a plot of $-\varepsilon_1$ vs λ^2. The existence of a straight line in this plot is characteristic of free electron-like behavior. The slope of the line is equal to $1/\lambda_p^2$, where λ_p is the wavelength associated with the plasma frequency. The data yield a plasma energy of 9.2 eV, which are used to generate $\tilde{\varepsilon}_f$ via the Drude model. The difference between the observed $\tilde{\varepsilon}$ and $\tilde{\varepsilon}_f$ is the interband component of $\tilde{\varepsilon}$. Ehrenreich and Philipp associate the lowest energy structure in $\tilde{\varepsilon}_{\text{interband}}$ to transitions from d-band to Fermi level at L in the Brillouin zone. The assignment is made with the aid of similar analyses of Cu.

The measurements and decomposition for Ag also provide evidence for the depression of the plasma frequency of Ag from the Drude result of 9.2 eV to 3.9 eV due to the onset of interband transitions. Plasma oscillations are approximately normal modes of the system of electrons. This implies that

$$\mathbf{E}^{\text{ext}} = \mathbf{D} = \tilde{\varepsilon}\mathbf{E} = 0. \tag{25}$$

Since $\mathbf{E}$ is not zero,

$$\tilde{\varepsilon} = \varepsilon_1 + i\varepsilon_2 = 0. \tag{26}$$

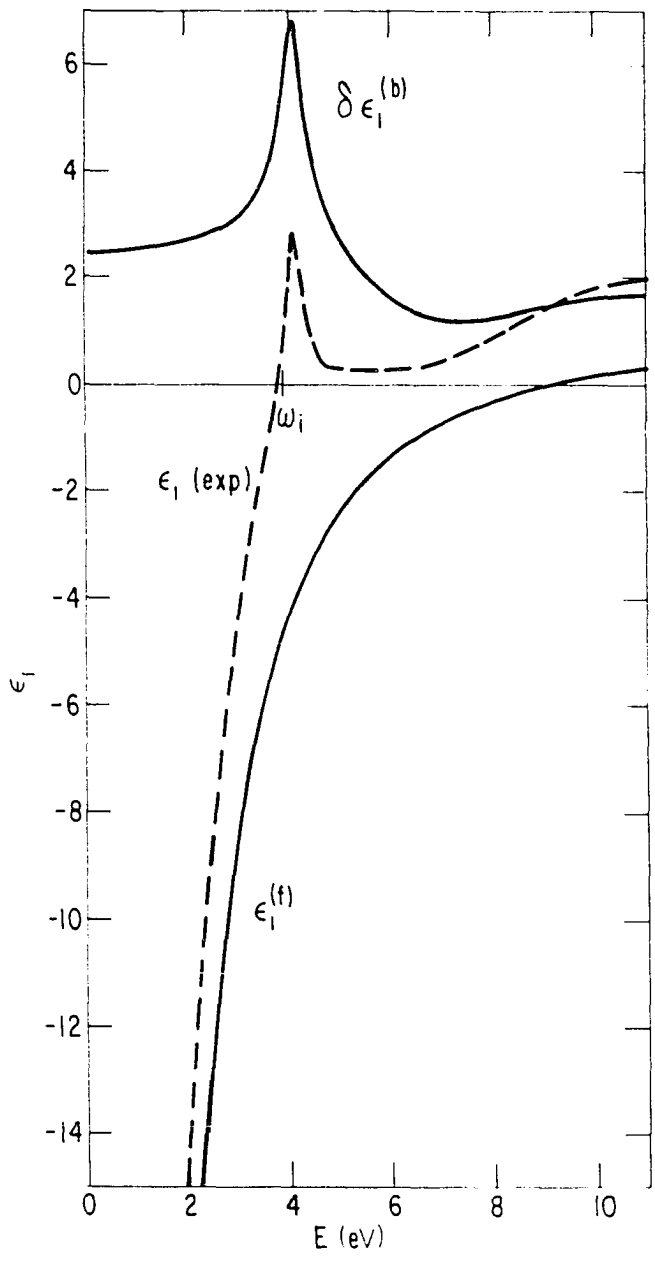

Figure 1: Decomposition of the experimental values of $\varepsilon_1(\omega)$ for Ag into free and bound contributions $\varepsilon_1^{(f)}$ and $\delta\varepsilon_1^{(b)}$. The threshold energy for interband transitions is indicated by ω_i. Reproduced from H. Ehrenreich and H. R. Phillip [2]

The plasma frequency will then occur where $\varepsilon_1 = 0$ and $\varepsilon_2 << 1$. Examination of the measured ε_1 for Ag shows that it does pass through zero slightly below the peak associated with the d-band to Fermi surface transition. The free electron plasma frequency is effectively depressed due to the presence of the onset of interband transitions. The reduced plasma frequency is referred to as the screened plasma frequency. It is effective at all energies below the onset of interband transitions in Ag.

The loss function ($\mathrm{Im}(-1/\tilde{\varepsilon})$) is an especially sensitive indicator of zeros in $\tilde{\varepsilon}$. Figure 2 shows the loss function for Ag derived from the n and k data of Johnson and Christy [3]. The screened plasma energy from this result is 3.78 eV, a result used in model calculations later in this study.

Electronic states and optical properties of metallic alloys

In earlier sections, the relationship between the optical properties of materials and their electronic states was discussed. The present study is of disordered metallic alloys, materials which by definition lack the translational symmetry characteristic of elemental crystalline solids. Theoretical models of ordered solids rely heavily on this symmetry to calculate the band structure of these solids. The band structure is intimately involved in the model dielectric function which is compared with observed optical properties.

Intraband absorption processes depend on the optical effective mass,

$$m^*_{opt} = 12\pi^2\hbar^2 N / \int_S d^3q \, \nabla^2 E_i(q) \qquad (27)$$

where N is the number of electrons per unit volume and the integral is computed over the Fermi surface. Interband absorption is more evidently

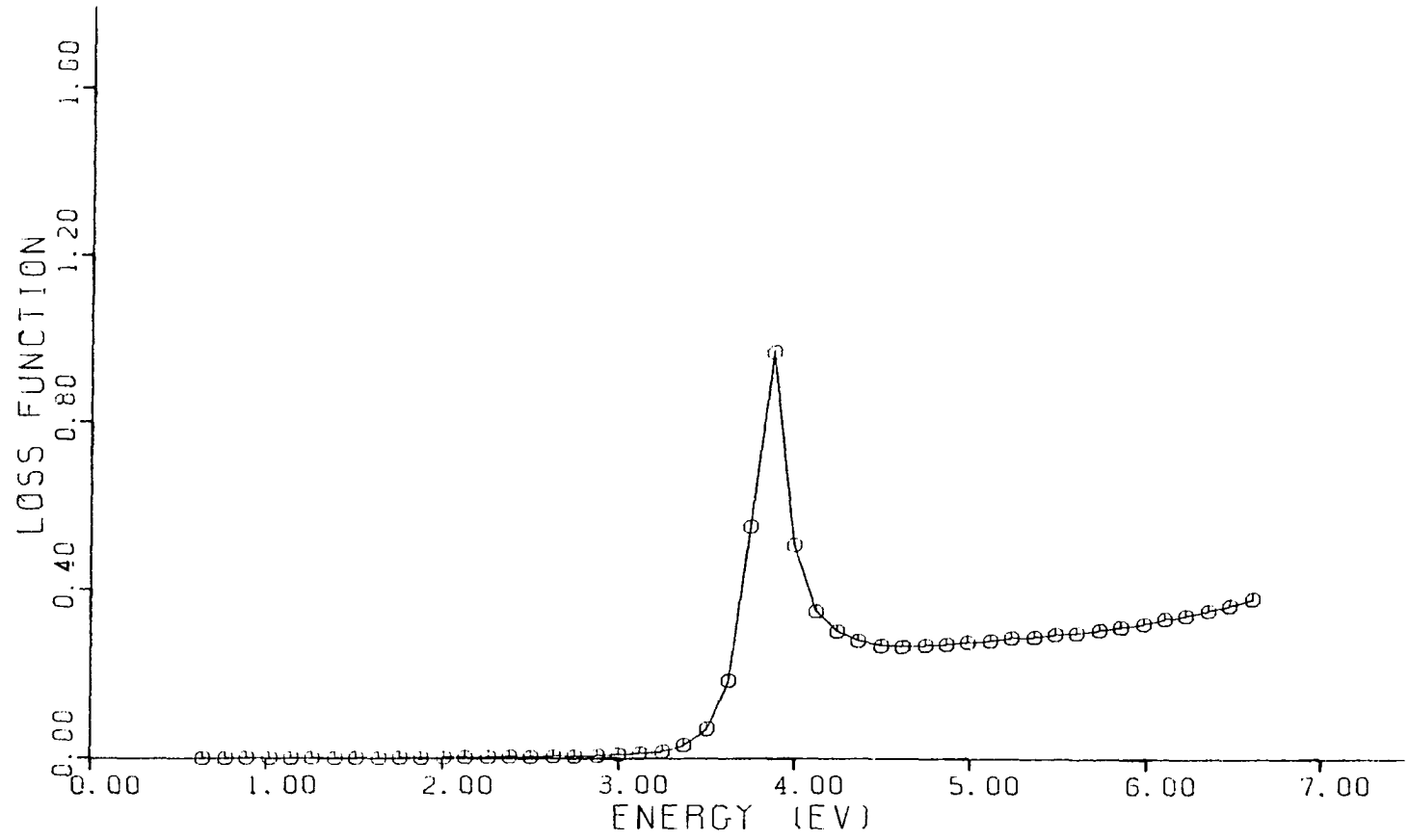

Figure 2: The loss function ($Im(-1/\tilde{\varepsilon})$) of Ag calculated from the data of Johnson and Christy [3]

related to band structure through both the JDOS and the optical transition matrix elements. It is evident that serious theoretical problems result when **q** is no longer a valid quantum number: band structure as we know it does not exist. As we mentioned earlier, however, the density of states remains a valid concept, since it is a function of energy only.

Dilute alloys should present the most tractable situation for theorists since small deviations from a calculable situation can be taken into account using perturbation theory. This is the starting point for models of electronic states in alloys.

Rigid band approximation In this simplest of models of alloys, the effect of the introduction of the solute atoms into the host is assumed to perturb all the electrons of the host system equally. Band structure is assumed to remain a valid concept. The result of the constant perturbation is to shift the energies of electrons in the system by a constant amount, thus retaining the shape of the band structure and density of states. The solute, however, will modify the electron density if the number of valence electrons is different than that of the host atoms. The result is a shift of the Fermi energy. This situation shows up very clearly in the optical properties since a shift in the Fermi energy will change the onset of interband absorption.

The rigid band model has been fairly successful in explaining the optical properties of dilute alloys of noble metals with polyvalent metals whose valence electrons have only s and p character. However, an important modification of the simple theory was required even in this

case. The original assumption that the electrons of the host experienced a constant perturbing potential was equivalent to assuming that the host and solute valence electrons simply merged and were uniformly distributed throughout the solid. Friedel [4] pointed out that such a situation cannot be the equilibrium case in a metal for situations where the number of valence electrons of the host and solute are not identical. In a metal, the conduction electrons would certainly distribute themselves in space so that the excess or deficit of charge due to the solute core would be screened from the rest of the solid. The theoretical treatment of this situation involves calculation of the phase shifts of scattering of conduction electrons by this local concentration of electrons. For solutes with only s and p valence electrons, the effect is to reduce the magnitude of the average perturbing potential. The main features of the model remain unchanged.

Virtual bound state model For the situation where the solute valence electrons have d-like character, the Friedel screening results in a quite different physical situation. The wavefunctions of impurity d electrons mix with the host conduction band wavefunctions to produce a localized (in space at the impurity site and in energy) band of states. The result in a non-magnetic alloy is a single peak in the density of states of the conduction electrons. Figure 3 illustrates the situation. Friedel [4] and Anderson [5] have shown that the change in shape of the density of states has a Lorentzian line shape that can be parametrized as

$$n_d(E) = \frac{10}{\pi} \frac{\Delta}{(E-E_d)^2 + \Delta^2} \tag{28}$$

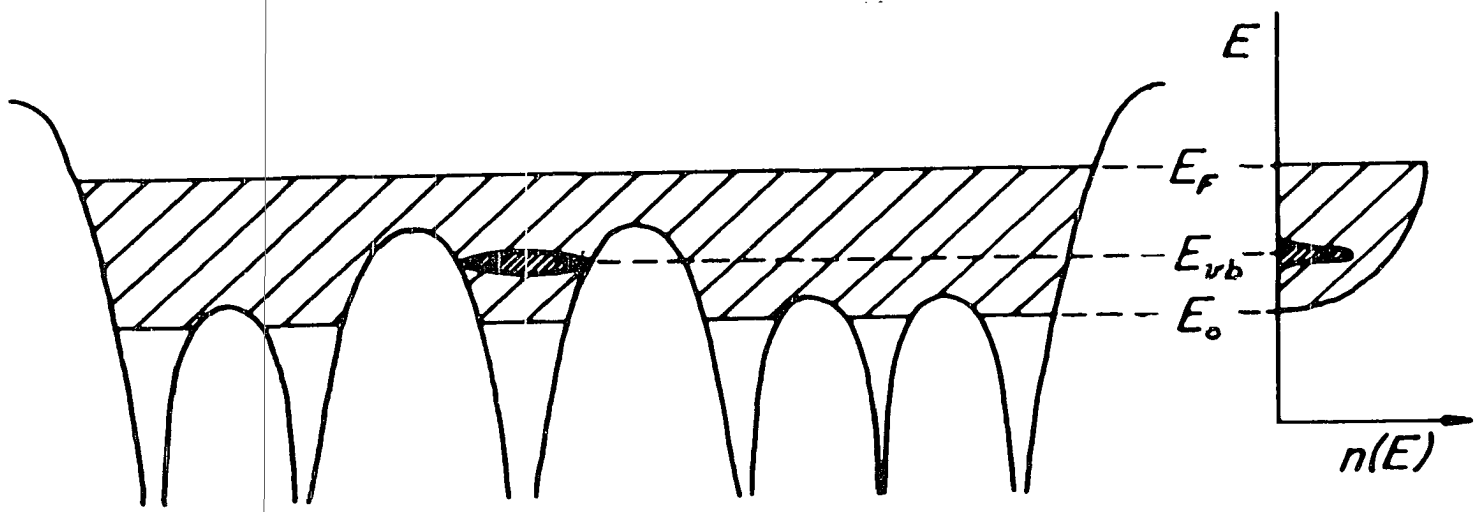

Figure 3: Schematic potential energy diagram of localized states in a dilute non-magnetic alloy and the associated density of states diagram, showing a virtual bound state at E_{vb}. Reproduced from D. J. Sellmyer [6]

The distribution is centered at E_d and has a halfwidth Δ. When E_d is close enough to the Fermi energy, the scattering of host electrons into impurity states at that energy adds an impurity term to the resistivity

$$\rho = \rho_{pure} + \rho_{impurity} \tag{29}$$

where

$$\rho = \frac{m^*}{ne^2} \frac{1}{\tau} \tag{30}$$

In this expression, m^* is the average effective mass of the conduction electrons and n is the electron density. Impurity concentration effects enter this expression through the additivity of electron inverse relaxation times.

$$\frac{1}{\tau} = \frac{1}{\tau_{pure}} + \frac{c}{\tau_i} \tag{31}$$

Using the Friedel approach $1/\tau_i$ is found to be

$$\frac{1}{\tau_i} = \frac{\Delta n_d(E_F)}{n_s(E_F)} \tag{32}$$

Here $n_s(E_F)$ is the density of host conduction electrons at the Fermi level. In Anderson's equivalent model,

$$\frac{1}{\tau_i} = \pi V_{sd}^2 n_d(E_F) \tag{33}$$

where V_{sd} is the s-d interaction matrix element. From this, it is apparent that

$$V_{sd}^2 = \frac{\pi\Delta}{n_s(E_F)} \tag{34}$$

At high frequencies ($\omega\tau >> 1$), the response of the electrons is described by the complex dielectric constant, $\tilde{\varepsilon}$, or complex conductivity, $\tilde{\sigma}$. Using the Friedel-Anderson model, both Caroli [7] and Kjöllerström [8] have computed $\tilde{\varepsilon}(\omega)$. Kjöllerström's expression for $\tilde{\varepsilon}(\omega)$ is

$$\tilde{\varepsilon}(\omega) = \tilde{\varepsilon}_f + \tilde{\varepsilon}_{sd}$$

$$\tilde{\varepsilon}_f = 1 - \frac{\omega_p^2}{\omega(\omega + i/\tau_p)} \tag{35}$$

$$\tilde{\varepsilon}_{sd} = \frac{c}{\omega^2}\left[\frac{\omega_p V_{sd}}{(\omega + i/\tau_p)^2} + \omega_d^2\right][L(\omega) + iA(\omega)]$$

Here $\tilde{\varepsilon}_f$ is the host dielectric constant and $\tilde{\varepsilon}_{sd}$ is the impurity contribution. The impurity contribution can be interpreted as arising from two processes: conduction electron scattering by impurity states (term containing V_{sd}) and direct interband transitions from impurity states (ω_d^2 term, ω_d is a parameter proportional to the d-s dipole matrix element). The functions L and A are given by

$$L(\omega) = -\frac{5}{2}\ln\frac{[(\omega+E_F-E_d)^2 + \Delta^2][(\omega-(E_F-E_d))^2 + \Delta^2]}{[(E_F-E_d)^2 + \Delta^2]^2}$$

(36)

$$A(\omega) = 5\left[\tan^{-1}\left(\frac{\omega + E_F - E_d}{\Delta}\right) + \tan^{-1}\left(\frac{\omega - E_F + E_d}{\Delta}\right)\right]$$

Beaglehole [9] has shown that this expression for $\tilde{\varepsilon}$, as well as Caroli's equivalent expression, are valid only for impurity concentrations that are immeasurably low. He demonstrated that for $\omega\tau_p \ll 1$, Kjöllerström's $\tilde{\varepsilon}$ is unphysical. Furthermore, he showed that while the correct shape of $\tilde{\varepsilon}$ is obtained for $\omega\tau_p \ll 1$, the magnitudes are incorrect.

Beaglehole discusses patches to the approach of Kjöllerström which yield more physical solutions for $\tilde{\varepsilon}$. He shows that the assumption of a frequency dependent impurity relaxation time removes Kjöllerström's low frequency difficulties. He also demonstrates that the high frequency

problem is associated with Kjöllerström's failure to renormalize the effective mass to be consistent with the sum rule

$$\int_0^\infty \omega \varepsilon_2(\omega) d\omega = \frac{1}{2} \pi \omega_p^2 \tag{37}$$

Since the integral represents the total absorption, he argues that renormalization is necessary whenever additional absorption is introduced. Virtual bound states clearly provide additional absorption. In this expression, the ε_2 is the interband ε_2 only. For $(E_F - E_d) \gg \frac{h}{\tau}$ or, when $(E_F - E_d)$ is small, for low concentrations such that $\frac{h}{\tau} \ll \Delta$, the change in effective mass in Beaglehole's approach is

$$\frac{m_r^*}{m^*} = 1 + c\alpha \tag{38}$$

where

$$\alpha = 5\, V_{sd}^2 \frac{(E_F - E_d)^2 - \Delta^2}{[(E_F - E_d)^2 + \Delta^2]^2} \tag{39}$$

More recently, Beaglehole [10] has found it necessary to include explicitly the s and p phase shifts in addition to the customary d phase shifts for his model of the frequency dependent relaxation time.

The virtual bound state model and dielectric function calculations are essentially phenomenological. It is not possible to predict VBS parameters using the model. Some first principles calculations for dilute Cu(Ni) alloys have been made. Stocks *et al.* [11] used the coherent potential approximation. Reidinger [12] and Cook and Smith [13] have used a single impurity (Greene's function) approach. Bassett and Beaglehole [14] report using Cook and Smith's approach to obtain reasonable agreement with data on Au(Ni).

The virtual bound state concept appears, at this time, to be the most fruitful for comparison of experiment with theory in the range of its applicability. The model provides separable points of comparison, in that the impurity induced interband absorption is separable from impurity induced changes in intraband absorption. Both of these effects have their respective concentration dependences.

Experimental studies of dilute noble metal : transition metal alloys

The first experimental optical observation of virtual bound states was reported by F. Abeles in 1962 [15]. He reported such states in alloys of Ni and Pd in Au. Reflectivity measurements, similar to Abeles' have been reported on a few other transition metal solutes in noble metals. Myers, Norris and Wallden [16] measured the transmission and reflection coefficients of Pd in Cu, Ag and Au, as well as Mn in Cu and Ag. Feinleib, Scouler and Hanus [17] measured the reflectivity of Ni in Cu. These studies were able to determine that structures attributable to virtual bound states did exist in Au for Ni and Pd solutes, in Ag for Pd and Mn, and in Cu for Ni, but not for Pd and Mn. Alloying in these systems did not change the onset of interband absorption in the host metal up to nearly 40 atomic % transition metal solvent.

The basic technique of these researchers was to measure the reflectivity of the pure noble metal and the alloy separately, compute $\tilde{\varepsilon}$ for each sample and subtract $\tilde{\varepsilon}_{pure}$ from $\tilde{\varepsilon}_{alloy}$. The remaining features are assumed to be characteristic of the alloy. The relative size of the structure made it possible to estimate virtual bound state positions in

Cu(Ni), Ag(Pd) and Ag(Mn). In most cases, the position was estimated from data taken on relatively high concentration alloys. The lowest reported concentrations were 5% Pd and Mn in Cu, both of which yielded no measurable VBS structure. Estimates of Δ were often not made and, when made, were usually much larger than those determined later by more sensitive techniques.

Two problems associated with this type of measurement have been evident. The reflectivity of noble metals and their dilute alloys in the infrared is high. Small deviations in reflectivity may easily be masked by noise. For example, a 20% change in absorptivity is equivalent to a 1% change in reflectivity when the absorptivity is 0.05. A more serious problem in Cu and Au based alloys is presented by the interference of host interband transitions near the region where VBS structure is observed. As a result, reflectivity measurements on dilute alloys do not exist and complete fitting of observed spectra to the VBS model is either impossible or questionable.

Photoemission experiments share some of the problems of reflectivity measurements. However, they have the advantage of being insensitive to the intraband structure. A first approximation to the interpretation of photoemission data is that the energy distribution curves (EDCs) map the structure of the density of occupied states of the sample. Like reflectivity and absorptivity measurements, photoemission experiments rely on observing the difference between EDCs of alloy and EDCs of the pure host material. Typically, EDCs are obtained for several incident

photon energies. Photoemission is valuable for identifying the position of structures due to direct transitions from filled states.

Norris [18] reports photoemission measurements on Mn in Cu and Ag and Pd in Ag. He observes no structure characteristic of the alloy in CuMn he estimates VBS structure at 3 eV in Ag(Mn) (observing that the other expected state must be above the Fermi level) and at 2 eV in Ag(Pd). Wallden, Seib and Spicer [19] have studied Ni in Cu and Mn in Ag. They report VBS structure in Cu(Ni) at 1.1 eV with Δ = 1.5 eV and a single VBS peak in Ag(Mn) at 2.6 eV with Δ = 3 eV. Because of sensitivity problems, no photoemission experiments have been reported on very dilute samples. The most dilute samples were 10 atomic %. VBS peak positions have been reported regularly, but Δ is not estimated with confidence.

The most reliable and reproducible measurements have been differential measurements. The various differential techniques are characterized by direct measurement of the difference in the measured quantity between pure host and alloy material. Phase sensitive electronics are capable of reliably measuring small signals that would otherwise be buried in noise. Three differential techniques have been used to study optical properties of dilute noble metal-transition metal alloys: differential ellipsometry, differential reflectivity, and differential absorptivity.

Drew and Doezema [20] used differential absorptivity to study Cu(Ni) alloys with Ni concentrations ranging from 0.5 to 3.7 atomic % Ni. They set the value of E_F-E_d at 0.72 eV with Δ = 0.25 eV. Beaglehole and Kunz

[21] utilized a differential reflectivity technique and obtained $E_F - E_d$ = 0.78 eV with Δ = 0.224 eV for Cu(Ni) with 1 - 2 atomic % Ni. Bassett and Beaglehole [14] used the same differential reflectivity technique to study Au(Ni) alloys having Ni concentrations in the range of 1-5 atomic %. They determined $E_F - E_d$ to be 0.495 eV for the lowest concentration sample with Δ = 0.129 eV. Lao, Doezema and Drew [22] used differential absorptivity on Au(Ni) (2 atomic % Ni) and determined $E_F - E_d$ = 0.47 and Δ = 0.108 eV. Callender and Schnatterly [23] are the only researchers to use differential ellipsometry. They measured Ag(Pd) with Pd concentrations ranging from 0.16 atomic % to 14.0 atomic %. For the lower concentrations of Pd they find $E_F - E_d$ = 1.93 eV with Δ = 0.25 eV. Bassett and Beaglehole [14] also report data from work of Lafait [24] and Theye [25] on Au(Pd) which they reanalyze. These data show that the differential measurements confirm each other despite differences in quantity measured. The repeatability led them to pursue more detailed comparison of the data with predictions of the VBS model.

Bassett and Beaglehole's work with data on these systems led them to propose the frequency dependent τ, s and p phase shift inclusion and renormalization of m^*_{opt} discussed in the preceding section. With these modifications, they were able to obtain excellent agreement with the modified VBS model for Ag(Pd), Au(Pd) and Au(Ni). Cu(Ni) remains anomalous in terms of the frequency dependent relaxation time. As a result of these differential measurements and the comparisons with the VBS model, there is no doubt that the model is useful for dilute noble metal-transition metal alloys.

Only one optical study of Ag(Ni) alloys has been reported. Koike, Yamaguchi, and Hanyu [26] have reported reflectance measurements on Ag(Ni) over the range 0.55 to 5.7 eV. Ni concentrations ranged from 1% to 11.8%. They claim to have identified a VBS peak at 1.8 eV with a Δ = 0.6eV. Ni in Ag forms a solid solution only up to approximately 1.5 atomic percent Ni. Koike, Yamaguchi and Hanyu prepared metastable solid solutions by coevaporating. The 1% Ni sample shows no detectable structure. Only the higher Ni concentrations show the 1.8 eV structure clearly. A second peak is observed below 0.5 eV. This peak is dismissed as a VBS peak because of the systematic changes in VBS parameters Koike reports for alloys of Ag with Ti, V, Cr, Mn, Co and Ni. They also note that the low change in DC resistivity for Ag(Ni) argues against a localized state close to the Fermi level. Their estimate of Δ for the 0.5 eV peak is 0.17 eV. This value is consistent with observations of Δ for Ni in Cu and Au.

These data share the problems of other pure reflectivity data. The measurements are worth repeating with more sensitive techniques. In addition, no solute has been measured in all of the noble metal hosts at dilute enough concentrations to permit systematic comparison of changes of VBS parameters as a function of host properties. Clearly, Ag(Ni) would provide a valuable link between the Au(Ni) case which is able to be explained by Beaglehole's modified VBS model and Cu(Ni) which is not. This study attempts to provide data comparable to that available on Cu(Ni) and Au(Ni).

EXPERIMENTAL APPARATUS AND PROCEDURE

The AC calorimeter designed and built for this experiment is closely modeled on that developed by O. D. R. Hunderi [27] at the University of Maryland. Functionally, the AC calorimeter consists of a Ge(Ga) bolometer attached to the back of a substrate upon which the experimental alloy and the pure metal reference thin films have been deposited. The electrical leads to the bolometer provide both a controllable heat leak to a cold finger maintained at liquid helium temperature and the physical means of support for the bolometer-substrate system. Light is chopped at the exit slit of a monochromator. The reference frequency derived from the chopper is electronically halved and used to trigger the driver circuit for a vibrating mirror. The mirror alternately deflects the light to the reference side and alloy side of the sample. Two lock-in amplifiers monitor the bolometer circuit: one tuned to the chopper frequency, the other to the mirror frequency. The ratio of the bolometer output at these two frequencies is proportional to the difference in optical absorptivity divided by the sum of the absorptivities. This is the quantity of interest in this study.

In the remainder of this section, the equipment described above will be treated with more detail. Each major subsystem will be described and analyzed where necessary. The bolometer itself will be studied both theoretically and as it functions in this particular application. Sample preparation will then be discussed. Finally, the data acquisition procedures used will be described.

Ge(Ga) bolometer

Bolometers have been used as detectors of infrared radiation since the late 19^{th} century. Their operation is based on the temperature dependence of electrical resistivity. When heated by absorbed radiation, the bolometer changes resistance. The effects of the resistance change on the bolometer circuit can be measured, yielding a quantitative measurement of the absorbed power. Figure 4 shows a typical bolometer circuit consisting of a power source, a load resistor and the bolometer itself. The voltage across the load resistor is monitored to detect the bolometer changes.

In 1961, F. J. Low [28] developed a liquid helium-3 cooled germanium bolometer which had both higher sensitivity and lower noise equivalent power (NEP). NEP is defined as the incident power which yields a signal-to-noise ratio of unity for a 1 Hz bandwidth. His bolometer was gallium doped, as is the one used in this study. However, his system operated at 2K.

Most early applications of bolometers used the bolometer as a direct infrared radiation detector. In 1970, O. D. R. Hunderi [27] reported the success of an AC calorimeter in which the bolometer was used to detect the power absorbed by an experimental sample. One of his uses of this system was to study dilute alloys of Fe in Au. His system demonstrated that Ge(Ga) bolometers could be used at 4.2K to study alloy systems. Because the present study is very similar in method to Hunderi's, his apparatus was the starting point for our design.

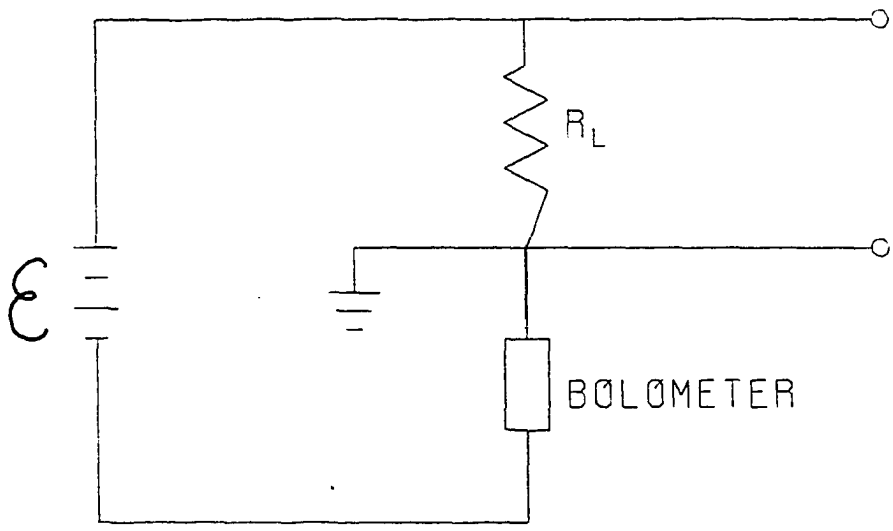

Figure 4: Typical bolometer circuit. The constant voltage supplied by the battery across the combination of the load resistor (R_L) and the bolometer. Resistance of the bolometer is a function of its temperature. The voltage across R_L is a function of the total current flowing in the circuit and, therefore, the power absorbed by the bolometer

Figure 5 shows the sample, substrate and bolometer. The bolometer is attached to the substrate with a thin coat of GE 7031 varnish. The two #30 AGW copper wires are soldered to the Ge(Ga) bolometer using indium solder applied with an ultrasonic soldering pen. The two insulated wires are clamped with two sheets of indium between pieces of OFHC copper which are part of the cold finger. In this configuration, the important parameters are the length of copper wire between the cold finger and the bolometer, the bolometer size and electrical characteristics, and the effective thermal mass of the sample-substrate-bolometer system.

Bolometer theory and practice In order to better understand the design criteria of the bolometer system, it is helpful to review briefly the theory of bolometer performance. Two approaches will be taken: one proceeding from electrical and thermal considerations and one from the point of view of electrical measurements only. The former better explains the interactions of the electrical and thermal characteristics, while the latter is the basis of evaluation of an existing bolometer system.

Bolometer theory from electrical and thermal properties Two properties of a bolometer system are of major importance: responsivity and NEP. Responsivity, which is symbolized by S to avoid confusion with resistance, is defined as the voltage produced by unit absorbed power,

$$S = \frac{dE}{dQ} \tag{40}$$

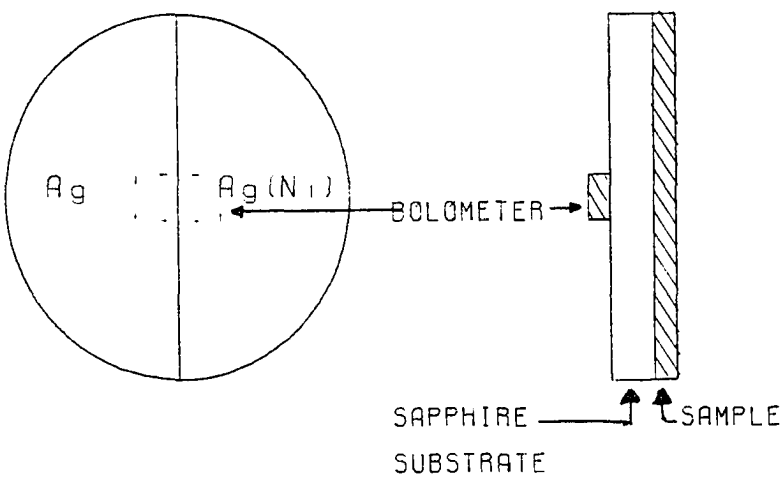

Figure 5: Schematic diagram of the sample-substrate-bolometer system

where E is the voltage across the bolometer element and Q is the radiant power absorbed. R. Clark Jones [29] demonstrates that for $Z_L >> Z$

$$S = \frac{\alpha E}{G - \alpha P}, \tag{41}$$

where α is the thermal coefficient of resistance of the bolometer material, G is the thermal conductance of the bolometer system and P is the electrical power dissipated in the bolometer.

Low [28] applies this for the static case to systems for which $R(T) = R_0(T_0/T)^A$ in the operating range and specifically models the Ge(Ga) system. With the substitution $\phi = T/T_0$, he finds

$$S = -\frac{A(\phi - 1)^{1/2}}{[(A+1)\phi - A][\phi^A]^{1/2}} \frac{R}{T_0 G}^{1/2}. \tag{42}$$

In his formulation R_0 and T_0 are the resistance and temperature when only background radiation is present. The quantity A is a property of the bolometer material near the operating temperature. Figure 6 shows plots of Equation (42) for several values of A. The pronounced maximum in the responsivity as a function of ϕ shows the importance of proper system design and choice of operating parameters.

In the static case, the final temperature of the sample-substrate-bolometer system depends on the thermal power to be dissipated at the bolometer and the thermal conductivity between the bolometer and the helium bath. Since the total thermal power to be dissipated is the sum of the joule heating and the absorbed radiation, the figure also demonstrates the importance of adjusting the bias current for maximum responsivity.

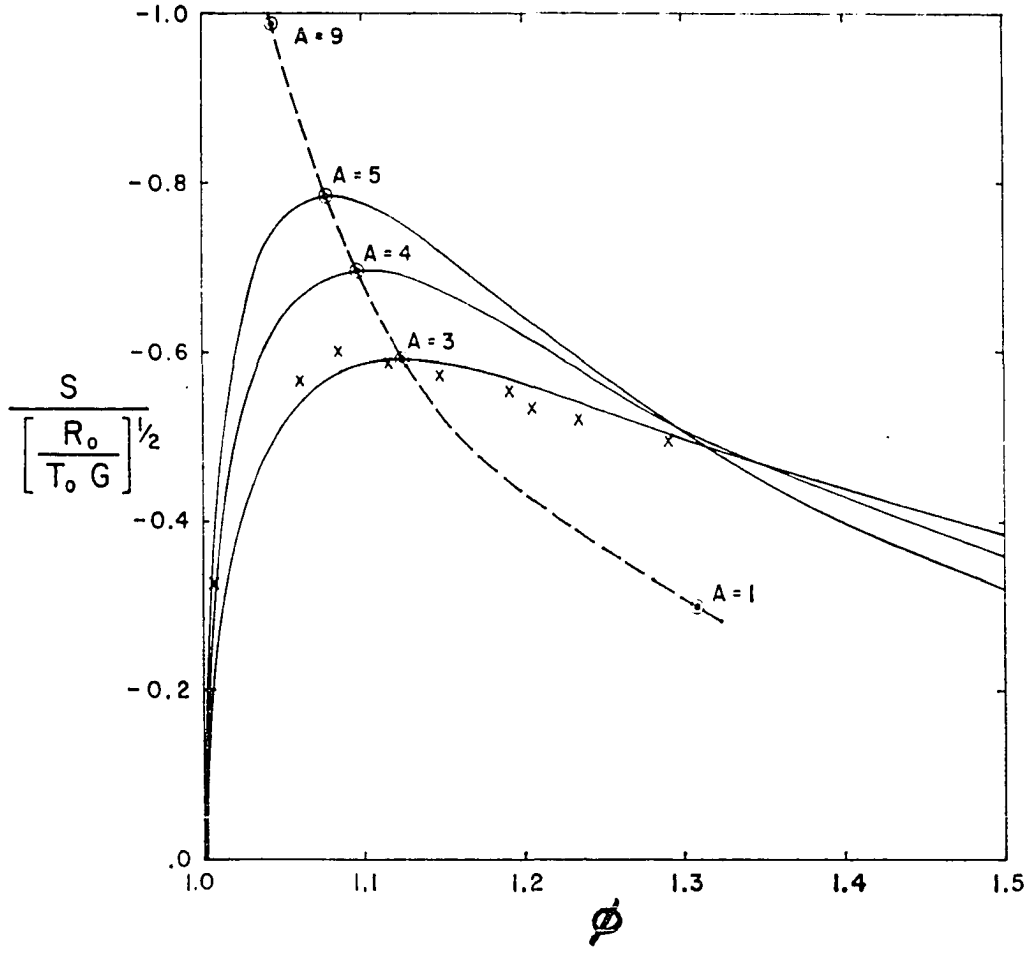

Figure 6: DC responsivity (S) as a function of reduced temperature (ϕ). Equation (42) is plotted for three values of A. The dashed line shows the position of the maximum for other values of A. Experimental points are shown for a bolometer with A = 3.85, G = 183 μW/K, $R_0 = 2 \times 10^4$ Ω, and T_0 = 2.15 K. Reproduced from F. J. Low [28]

While bolometers can certainly be used for static or DC measurement of absorbed power, certain situations call for AC measurement. When the experimental signal is expected to be small, it must compete with noise sources in the system. Electrical noise exists across the entire frequency spectrum, so that broad-band detection mechanisms will measure both the noise and experimental signal. The typical way of dealing with this situation is to modulate or chop the incident radiation at a specific frequency and detect with electronics which reject all frequencies outside a narrow band centered on the chopping frequency. If the modulation frequency and bandwidth are chosen properly, the signal-to-noise ratio can be raised sufficiently to permit small changes in experimental signal to be observable.

The thermal characteristics of the bolometer system are of much greater importance in this AC case. Specifically, the effective heat capacity of the system, the effective thermal conductance of the link to the helium bath and the chopping frequency of the light source are factors in determining the temperature changes responsible for the measured signal across the bolometer. Zwerdling, Smith and Theriault [30] have modeled this case for germanium bolometers.

In the AC case, the instantaneous power absorbed by the bolometer can be written as

$$q = q_0(1 - e^{i\omega t}) \tag{43}$$

where ω is the chopping frequency of the incident light. In response to this absorbed power, the instantaneous temperature of the bolometer can be written in similar form,

$$\delta = \delta_o(1 - e^{i\omega t}) \tag{44}$$

where the quantity $\delta = T - T_o$. Using these instantaneous quantities, a dynamic heat flow equation can be written:

$$C\frac{d\delta}{dt} + G_e\delta = q \tag{45}$$

In this equation, C is the dynamic thermal capacitance and G_e is the effective dynamic thermal conductance. The quantity G_e is not identical to the thermal conductance in the static case. Because of the changes in biasing power with changing temperature of the bolometer element, the apparent temperature changes of the bolometer element will be greater than that predicted assuming absorbed radiation to be the only periodic source of thermal energy for the bolometer system. For negative bolometers (materials characterized by $\alpha < 0$), G_e is always greater than the static thermal conductance.

Solving the dynamic heat flow equation yields a relationship between q and δ:

$$q = i\omega C(\delta - \delta_o) + G_e\delta \tag{46}$$

If a complex effective dynamic thermal conductance is defined as

$$G_e(\omega) = \frac{dq}{d\delta} \tag{47}$$

and this definition is applied to Equation (44), we obtain

$$G_e(\omega) = G_e + i\omega C \tag{48}$$

The magnitude of $G_e(\omega)$ can then be written as

$$|G_e(\omega)| = G_e(1 + \omega^2\tau_r^2)^{1/2} \tag{49}$$

where τ_r is the response time constant,

$$\tau_r = \frac{C}{G_e} \tag{50}$$

The response time constant includes both electrical and thermal effects. For negative bolometers the response time constant will be greater than the corresponding thermal time constant whenever the load resistance is not much greater than the bolometer resistance.

Using the expressions for instantaneous temperature rise and absorbed radiant power and considering the r.m.s value of both the AC voltage and radiant power absorbed, Zwerdling, Smith and Theriault then show that the apparent frequency spectrum of the responsivity of the system is

$$S(\omega) = \frac{S(0)}{(1 + \omega^2 \tau_r^2)^{1/2}} \tag{51}$$

In this expression, S(0) is the zero frequency responsivity of Equation (40), ω is the angular frequency of the external power source (the chopping frequency, not the frequency of the light), τ_r is the response time constant. For a given response time constant, the responsivity decreases as chopping frequency increases. The rate of this decrease is governed by the time constant, which is a function of the effective thermal capacitance of the system and the effective thermal conductance.

In a situation such as the one in this study, the expected oscillation range in absorbed radiant power is expected to be small. It is important, therefore to design the effective thermal capacitance of the sample–substrate–bolometer system to be as small as possible. Practical limits are imposed on the system design by the necessity for the sample to be in thermal contact with the bolometer. For minimum C, the sample–substrate–bolometer system should be as small as possible and

be constructed from materials having low specific heat. Once C is chosen by the design and construction of the system, the thermal conductivity of the link to the helium bath can be determined. A fundamental criterion for this choice arises from the requirement that full modulation of the temperature changes must be permitted. This implies that

$$\tau = \frac{1}{2\pi f} \tag{52}$$

or

$$G = 2\pi f C \tag{53}$$

Lock-in detection of the bolometer signal places another restraint on design. Noise rejection characteristics of lock-in amplifiers are significantly worse at very low frequencies. It is desirable to work with signals greater than 10 Hz whenever possible.

Noise equivalent power (NEP) is also an important property of bolometer systems. H. D. Drew [31] carefully considered the sources of noise for bolometer systems where the bolometer is used as a direct infrared detector. He identifies four important sources of noise:

1. Johnson noise of the bias resistor and input resistor to the amplifier.
2. Temperature noise. This is noise caused by the random fluctuations in the phonon flux between the detector and bath via the thermal link.
3. Photon noise resulting from fluctuations in the flux of electromagnetic radiation at the detector from the source and from the room temperature background.
4. Current noise found in certain types of resistors.

His calculations and measurements indicate that for a given operating temperature, NEP can be minimized by choosing the bias current to produce the maximum responsivity.

Hunderi correctly points out that experimental apparatus such as the one described here cannot have as low NEP as a free bolometer like Drew's. The larger absorber surface more efficiently collects background radiation, increasing photon noise, and the larger thermal mass requires a larger thermal link to the helium temperature bath, reducing sensitivity. At 4 K Hunderi found an NEP of 2.7×10^{-9} W. This is to be compared to Drew's 1×10^{-10} W NEP.

The calculations and experience of Drew and Hunderi suggest that it is important to use as high an operating frequency as possible to avoid Johnson noise and to use a helium-cooled load resistor. Background radiation should be limited as much as possible.

Measuring bolometer performance using the load curve While the preceding treatment of the bolometer theory is useful for understanding the interaction between the thermal and electrical characteristics of the system, direct measurements of the thermal parameters are not easily accomplished when the bolometer system is assembled for use. Zwerdling, Smith and Theriault [30] have shown, however, that the most important operational characteristics can be determined from bolometer load curve data. This is especially useful for optimization of bolometer performance immediately prior to experimental use.

After cooling the bolometer to liquid helium temperature, a continuous measurement of voltage (E) as a function of the bias current (I) is made. This smooth curve, the load curve, relates instantaneous values of E and I. From these values the static resistance, R, the dynamic resistance or impedance, Z, and the electrical power dissipation, P, can be calculated using

$$R = E/I \tag{54}$$

$$Z = dE/dI \tag{55}$$

and

$$P = EI. \tag{56}$$

Figure 7 shows the load curve of a bolometer used in the final measurements of this study. Figure 8 shows R and Z as functions of I for this same bolometer system. The zero frequency responsivity can be expressed in terms of these quantities alone:

$$S(0) = (Z-R)/2E \tag{57}$$

Figure 9 shows the responsivity of a function of I. This particular detector exhibits a maximum responsivity of 1.8×10^4 V/W at 10 μA bias current.

While the dynamic thermal conductance cannot be determined from load curve data alone, Zwerdling, Smith and Theriault show that

$$G_d = \alpha P \frac{Z + R}{Z - R} \tag{58}$$

Earlier measurements made on the bolometer material used in this study show that $\alpha = -1.5$ at 4.2 K. Figure 10 shows a plot of G_d as a function of the bias current. At 10 μA bias current the dynamic conductivity is approximately 500 μW/K. The design estimate of the thermal conductance

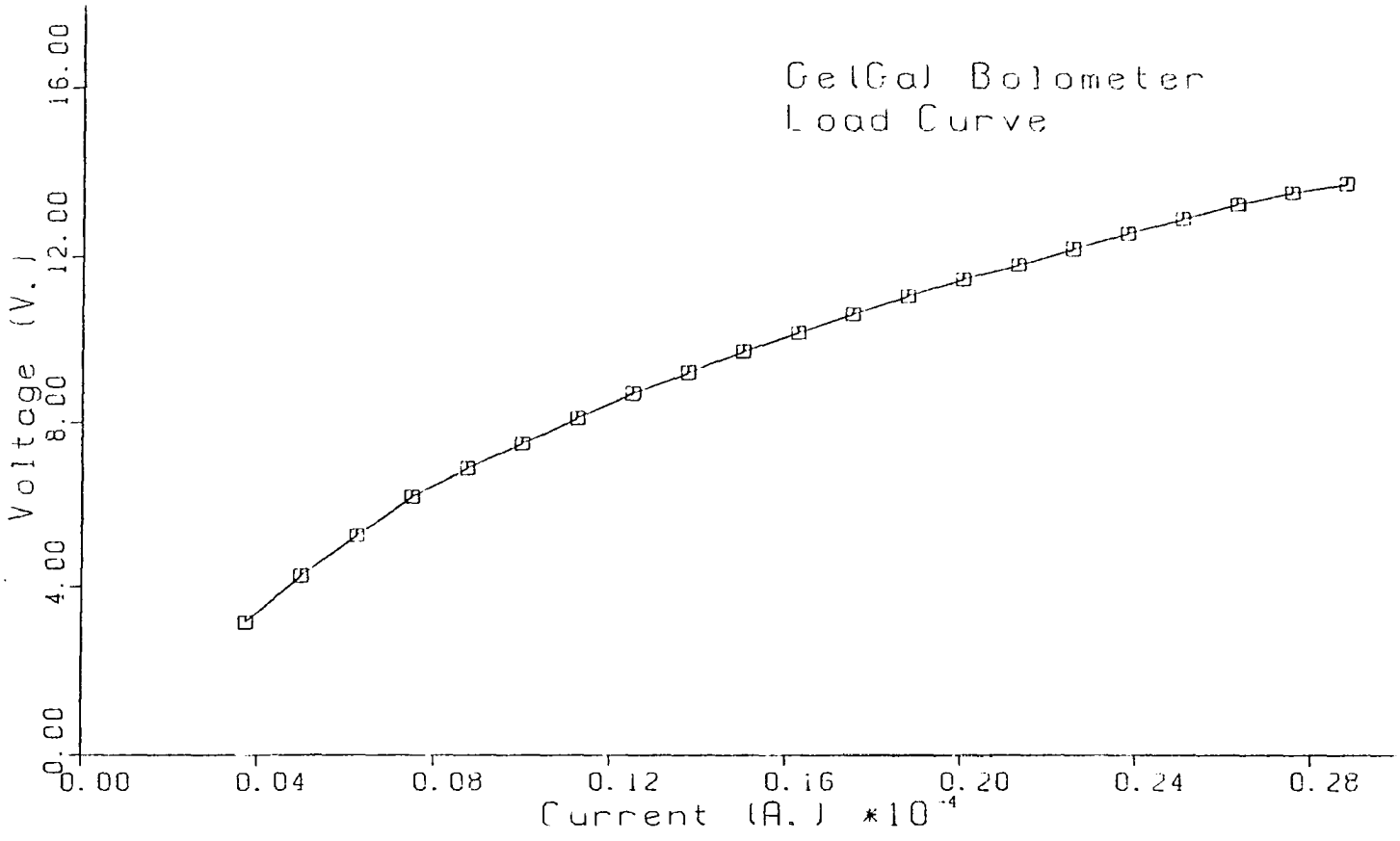

Figure 7: Bolometer load curve. These data were obtained from the bolometer used in the measurements for this study

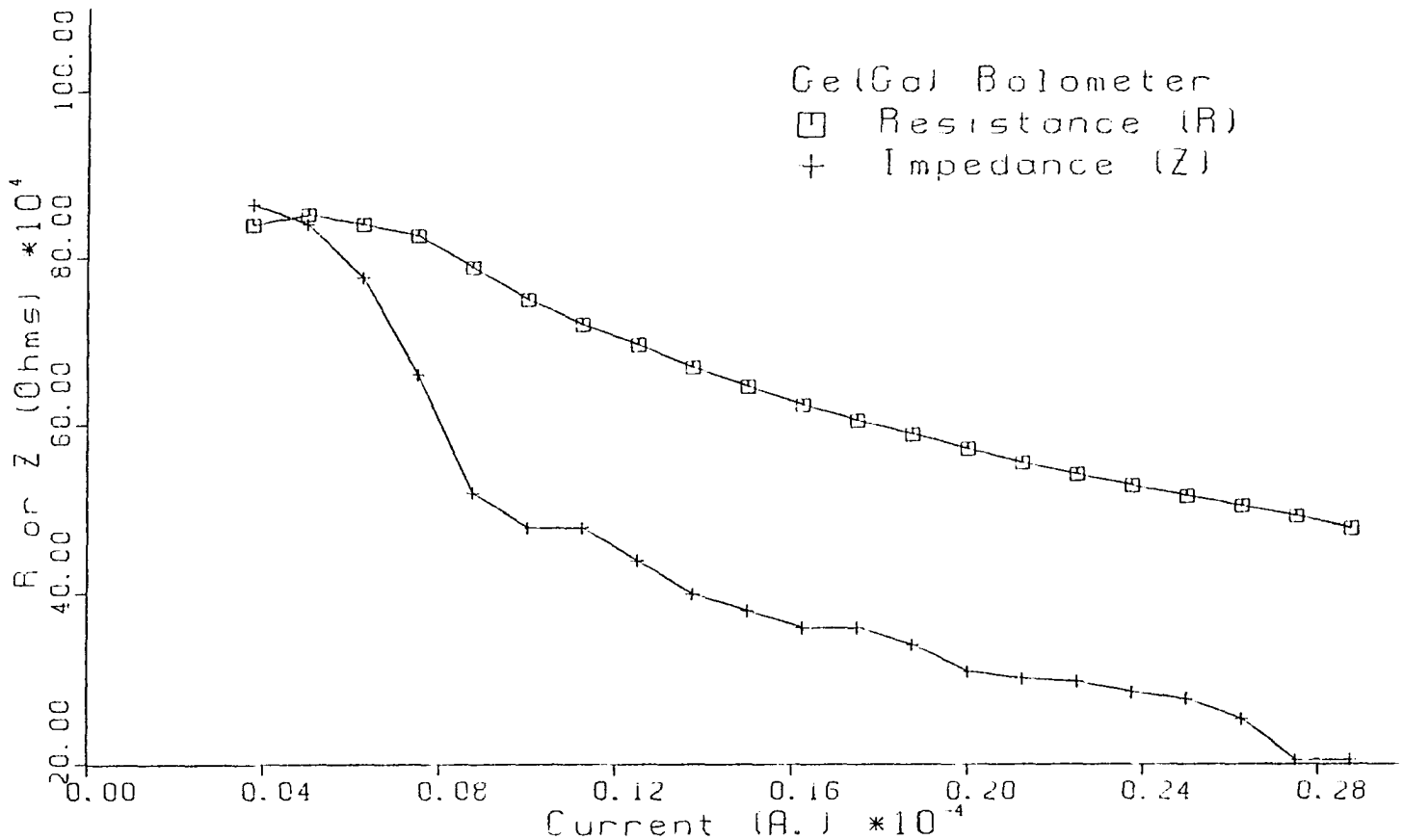

Figure 8: Resistance (R) and impedance (Z) of Ge(Ga) bolometer as a function of bias current. These data are calculated from the load curve of Figure 7

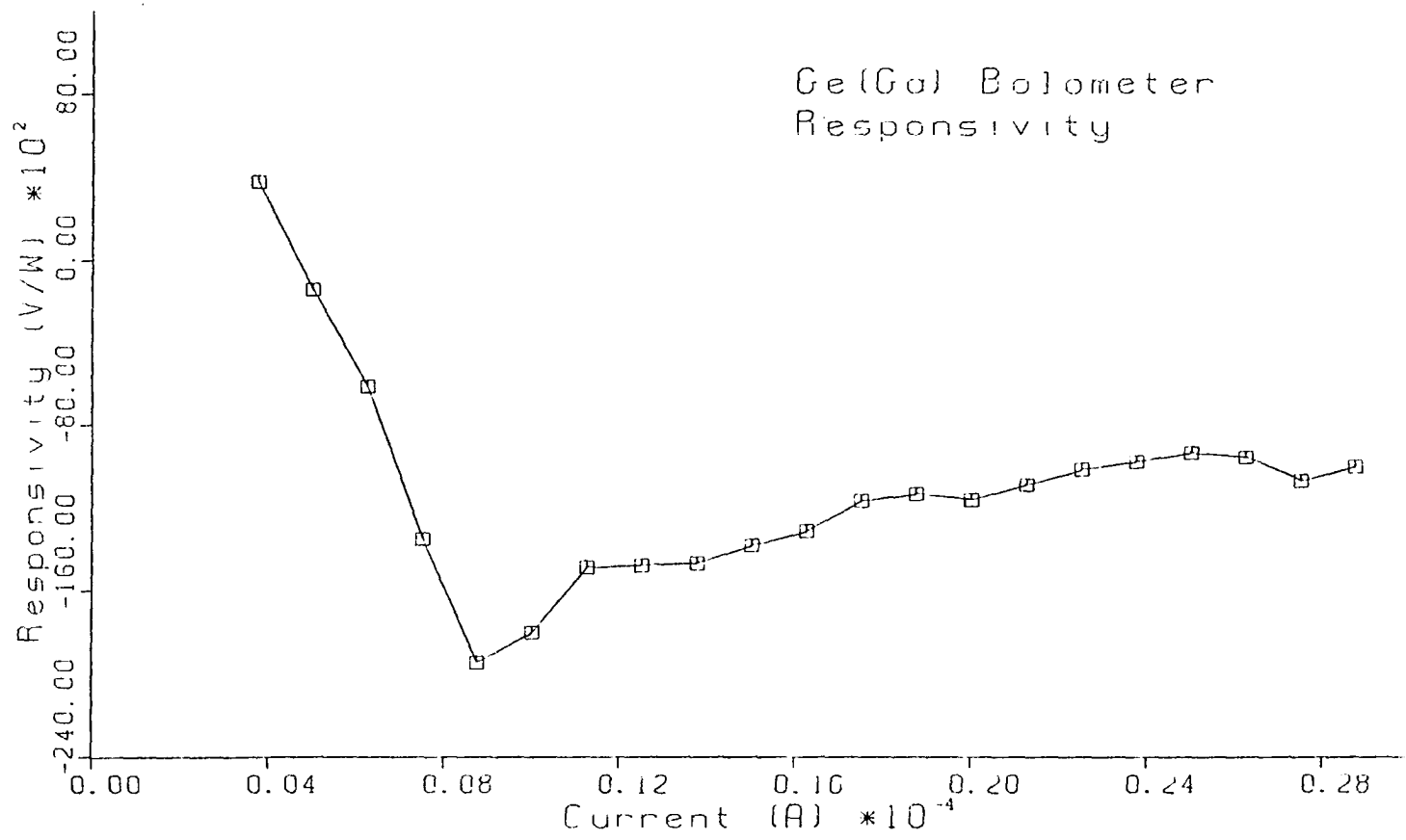

Figure 9: Responsivity (S) of Ge(Ga) bolometer as a function of bias current. These data are calculated from the load curve of Figure 7

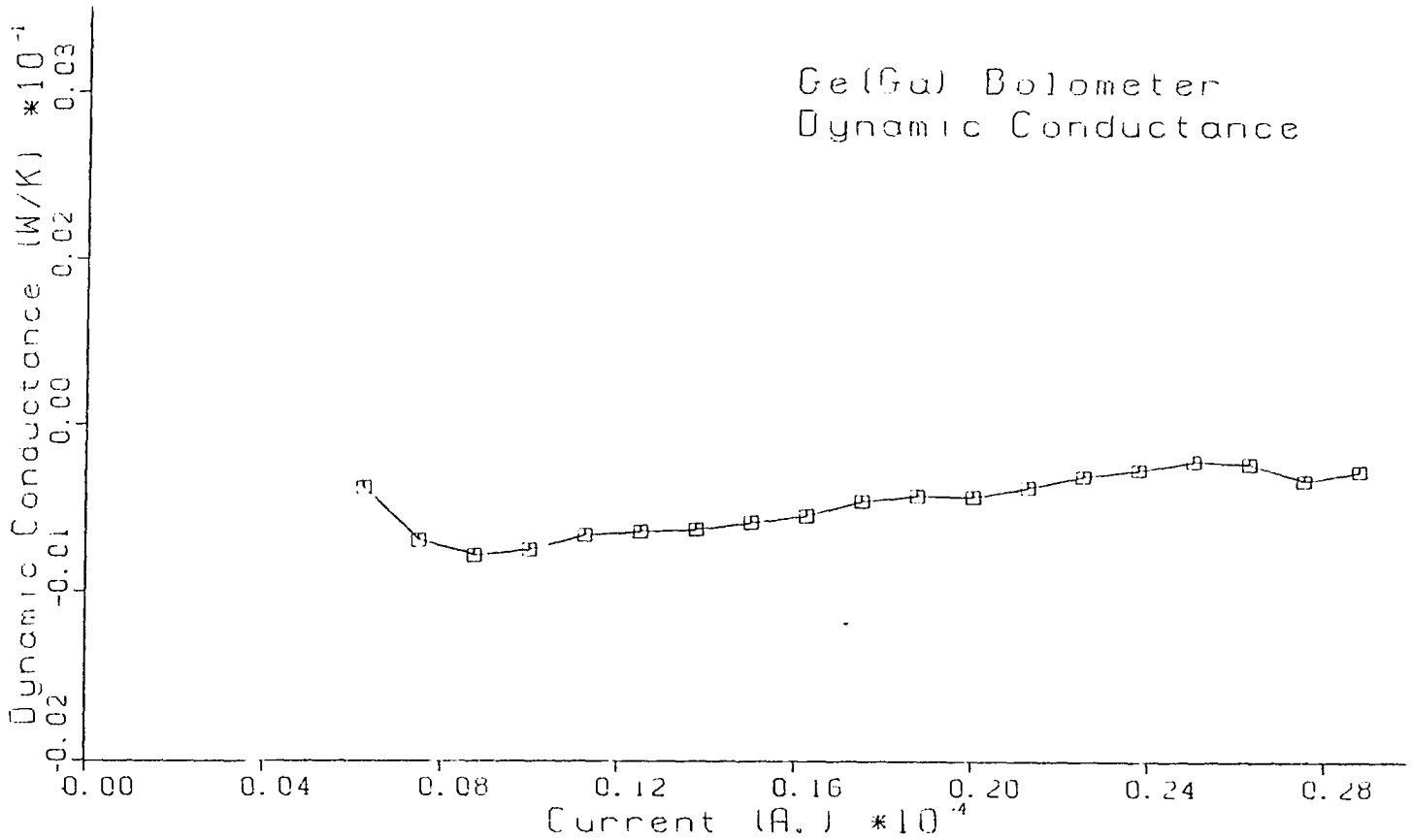

Figure 10: Dynamic conductance (G_d) of Ge(Ga) bolometer as a function of bias current. These data are calculated from the load curve of Figure 7

of the copper wires that provide the heat leak to liquid helium bath was 0.15 W/K.

The thermal time constants also cannot be determined from load curve data alone. In this case, the frequency dependence of the responsivity must be determined. An estimate of the time constants is available from the observation that adjustment of the frequency of chopping the light yielded a maximum signal between 15 and 20 Hz. For this maximum to be very near the zero frequency responsivity case, τ_r is on the order of 2×10^{-3} sec. A rough calculation of the thermal time constant yields $\tau_{th} = 10 \times 10^{-3}$ sec. This is good agreement especially recognizing that $\tau_{th} > \tau_r$ whenever the load resistance is not equal to the bolometer resistance.

Calculations based on the load curve data indicate that the bolometer used in this study is comparable to that used by Hunderi. The zero frequency responsivity is slightly larger than his, probably because of the substitution of sapphire for mica substrates. No measurement of NEP was made for comparison.

Bolometer system cryostat

The cryostat used for this study was originally designed to permit in-situ evaporation of alkali metals. For this reason, the cryostat (see Figure 11) is stainless steel to permit baking during room temperature pump down. This is necessary to achieve the ultrahigh vacuum required for the study of alkali metals. The cryostat is also longer than normal so that the original liquid helium cold finger could be lowered into position for evaporation of the alkali film. The vacuum pumps were also chosen to reduce contamination. A carbon vane pump was employed to rough

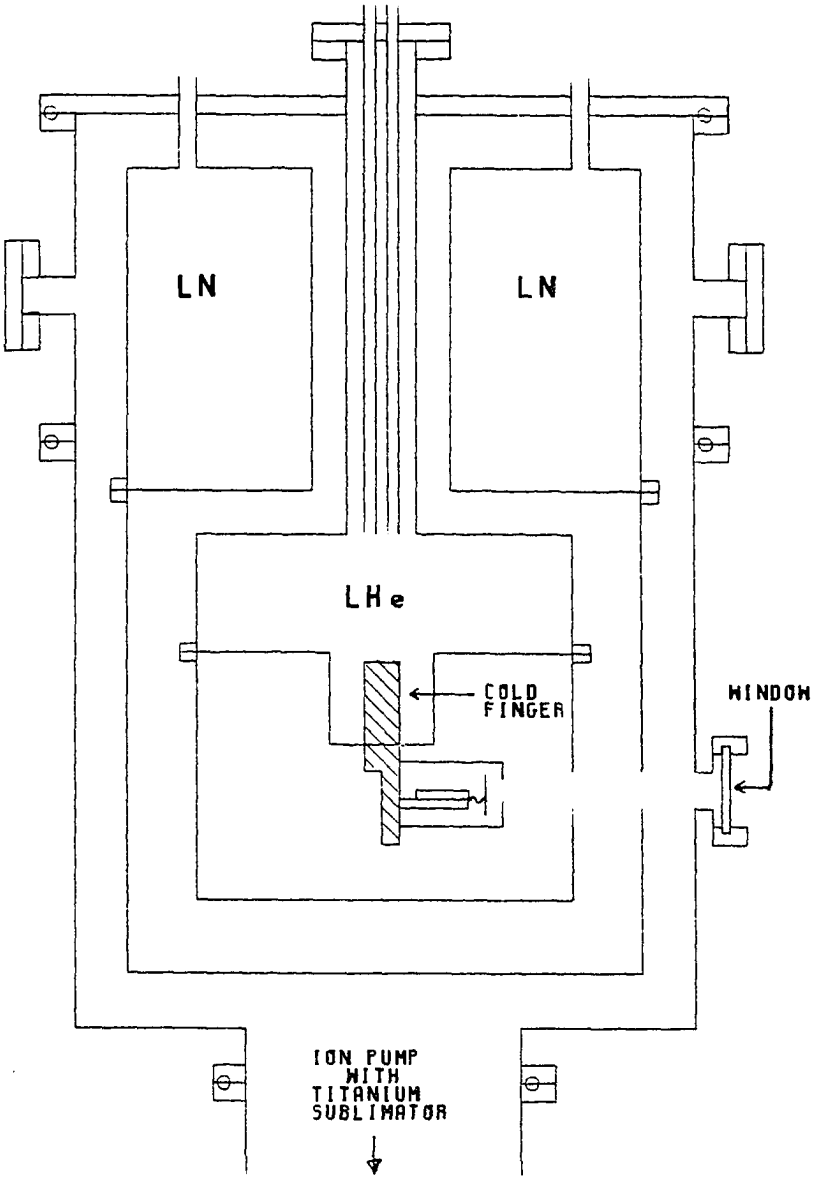

Figure 11: Schematic diagram of LHe-4 cryostat used in this experiment

the system to the point that the Varian sorption pump could begin to pump effectively. The sorption pump was capable of lowering the pressure to the point that the Varian ion pump with its titanium sublimator could be started. A second ion pump was mounted on one of the small flanges near the top of the cryostat for improved pumping speed. Despite the second ion pump and periodic attempts at baking the system, the system only pumped to the 10^{-6} Torr range at room temperature.

For this study, the cryostat was modified by installing a large OFHC copper cold finger which extended through the base of the helium container into the liquid helium bath itself. Slots were milled into the cold finger to increase the amount of surface in contact with the liquid helium. On the vacuum side, the cold finger was milled to permit the sample holder to be securely attached and kept in thermal contact.

The copper liquid nitrogen (LN) and liquid helium (LHe) temperature radiation shields were bolted to the respective vessels with a thin coat of Apiezon N to assure good thermal contact. Sodium chloride windows could be mounted in the holes that permitted light to reach the sample. However, in the final runs the windows were removed for easier optical alignment. The small radiation shield that was Woods-metal soldered to the sample holder was sufficient to reduce the background radiation to an acceptable level. The two small slots (approximately 1 cm by 3 mm) were just large enough to pass the nearly focused beam.

Electrical leads entered the cryostat at the top through Teflon thermocouple feedthroughs. To reduce thermal conductivity, #24 AGW manganin wires were used. The wires were wrapped around the liquid

nitrogen vessel, fed through to the liquid helium vessel where the LN temperature radiation shield was attached, wrapped around the liquid helium vessel both outside the LHe radiation shield and inside the shield, and finally terminated near the cold finger. In addition to the three leads required by the bolometer and its load resistor, four more were connected to a carbon resistor mounted in a hole in the cold finger. This resistor was used to monitor the temperature of the cold finger.

Because of the large copper radiation shields, the cryostat was not extremely efficient in its consumption of liquid helium. The relatively high boiloff rate during initial cool-down caused temperature oscillations in the long neck of the helium vessel. To eliminate this a series of baffles was installed. With this improvement, 4 to 6 hours of operation were possible after permitting 2 hours for the system to reach thermal equilibrium.

Sample preparation

Bulk samples of two Ag(Ni) alloys were prepared by F. A. Schmidt of the Ames Laboratory Metallurgy Division. Buttons of the alloy were prepared in a water-cooled, non-consumable arc furnace in an argon atmosphere. The samples were turned and remelted 8 times to insure uniformity. Samples with nominally 0.25 and 0.75 atomic percent Ni in Ag were prepared in the same manner.

Each of the buttons was then rolled into a 0.010 inch sheet from which a 5 inch diameter circular piece was cut. The circular piece of alloy was bonded to a stainless steel plate of the same diameter using an electrically-conducting epoxy. This became the target for rf sputtering

of the alloy. The process was repeated for both alloy targets and a pure Ag target. Prior to use in the rf sputtering system, the targets were etched in a solution of 5 parts NH_3OH and 3 parts H_2O_2, rinsed in deionized water and vapor degreased using isopropyl alcohol.

The substrates used were single crystal sapphire polished on one side. The 1 inch diameter, 0.020 inch thick substrates were purchased from Adolph Meller Company. The blank substrates were ultrasonically cleaned in acetone and methanol and vapor degreased in isopropyl alcohol prior to film deposition. A 200 Å layer of Cr was evaporated onto the substrate before rf sputtering of the Ag and Ag(Ni). This eliminated the problem of pinholes in the Ag and Ag(Ni) films.

The rf sputtering was done by James Anderegg of Dr. Danielson's group in the Solid State Physics Division of the Ames Laboratory. The substrate holder was cooled by a 21 l/min flow of liquid nitrogen boiloff gas. The sputtering rate was approximately 200 Å/minute using 200 W of rf power and Ar as the discharge gas. Deposition continued until the Sloan thickness monitor indicated a 2000 Å film thickness. The pure silver half of the masked substrate was deposited first. After removing the substrate and holder from the sputtering system to rotate the mask and change the target, the alloy was sputtered on the other half of the substrate. The samples were mounted on the bolometer and cryostat pumpdown initiated within an hour of removal from the sputtering system.

After the AC calorimeter measurements had been completed, the samples were electron microprobe analyzed to determine the actual composition of the films. These data were taken and the analysis

performed by F. C. Laabs of the Analytical Chemistry Group II. Table 1 summarizes the results of the analysis for the two samples discussed later.

Table 1: Electron Microprobe Analysis of Thin Film Samples of Ag(Ni) alloy rf Sputtered from the Ag (0.75 at % Ni) Target

	Ag (at. %)	Ni (at. %)
Sample 1	99.40 ± 0.07	0.60 ± 0.01
Sample 2	99.50 ± 0.03	0.50 ± 0.01

AC calorimeter system optics

Figure 12 shows the optical elements of the AC calorimeter system. Two light sources were used to cover the range of interest in this study: a globar for the infrared and a quartz iodine lamp for the visible and near ultraviolet. These sources were focused on the entrance slit of a Leiss double prism monochromator. CaF_2 prisms were used in this monochromator for the 0.3 to 0.8 eV range while quartz prisms covered from 0.5 to 3.3 eV. This monochromator has an effective relative aperture of f/6.4 to f/7.2.

A variable speed chopper was placed between the exit slit of the monochromator and the entrance of a baffled enclosure which reduced the amount of room light which could enter the cryostat. A 30 cm focal length concave front surface mirror focused the light in the plane of the

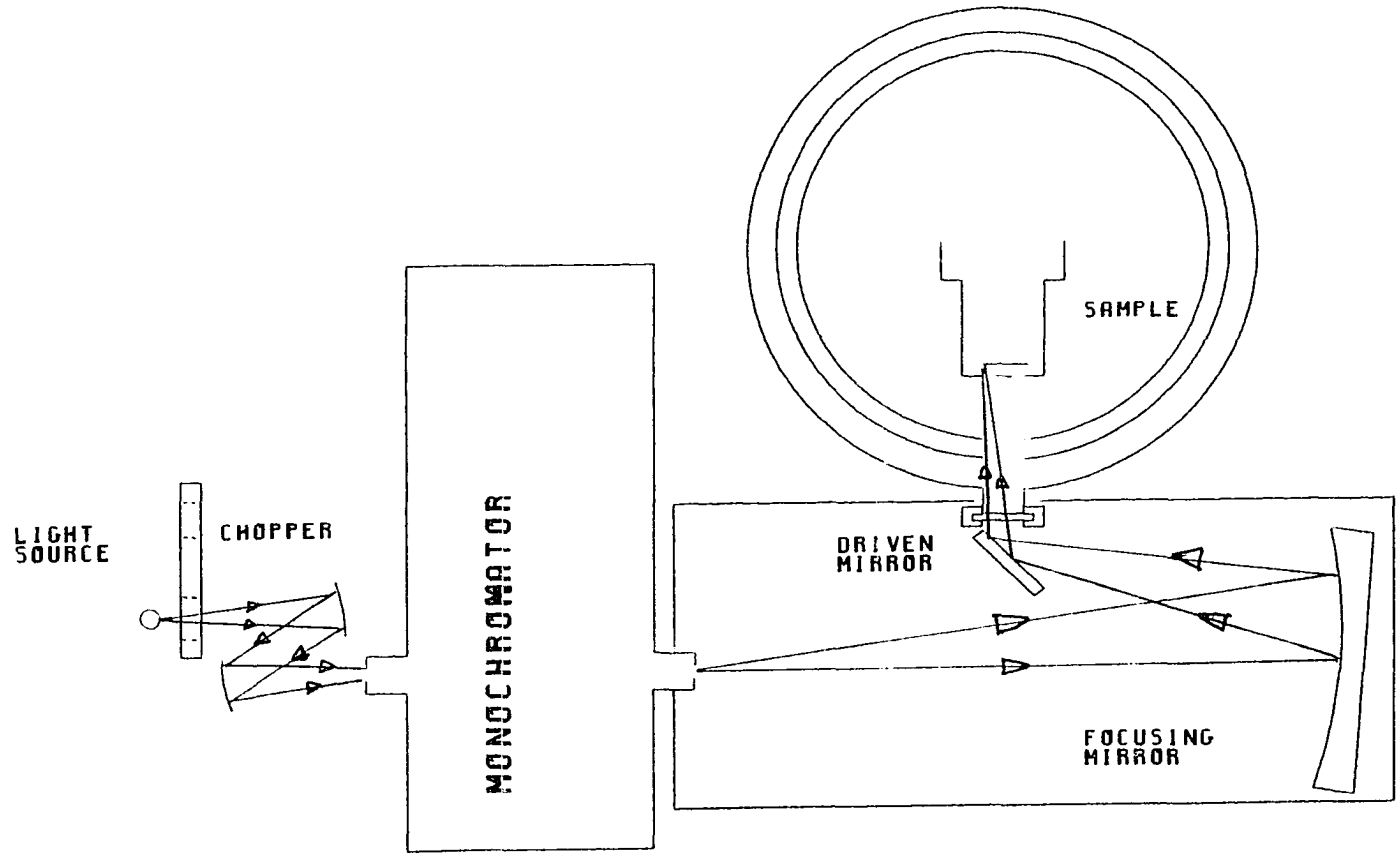

Figure 12: Schematic diagram of the optical elements of the AC calorimeter

sample. The deflecting mirror is driven at exactly half the frequency of the chopper to position the 1:1 image of the monochromator's exit slit alternately on the alloy side and the reference side of the sample.

Figure 13 is a detailed view of the driven deflecting mirror. The aluminum front surface plane mirror has a 1/16 inch diameter piece of stainless steel tubing attached to its back surface. The tubing and mirror are suspended from the upper support by a wire which is clamped above the support. Teflon guides keep the tubing from wobbling. Two ceramic permanent magnets cut from magnetic stirring bars are also attached to the back of the mirror so that they extend into the two solenoids mounted in the stationary back plate of the mount. These solenoids are driven by the trigger circuit such that the mirror is alternately held against the two stops provided by set screws. All mirror movement takes place during the time that the light beam is interrupted by the chopper.

This same trigger circuit provides the reference signals for the two lock-in amplifiers. The input to this circuit is a square wave produced by the photodiode reference pickup on the chopper. The position of this assembly can be adjusted such that the reference signal is in the proper phase relation to the chopped light. This adjustment is important since it provides the mechanism for assuring that the mirror moves only when the light beam is interrupted by the chopper. After halving the frequency of the reference signal, the power section of the circuit alternately closes sets of reed relays which control the direction of current flow through the solenoids on the mirror support.

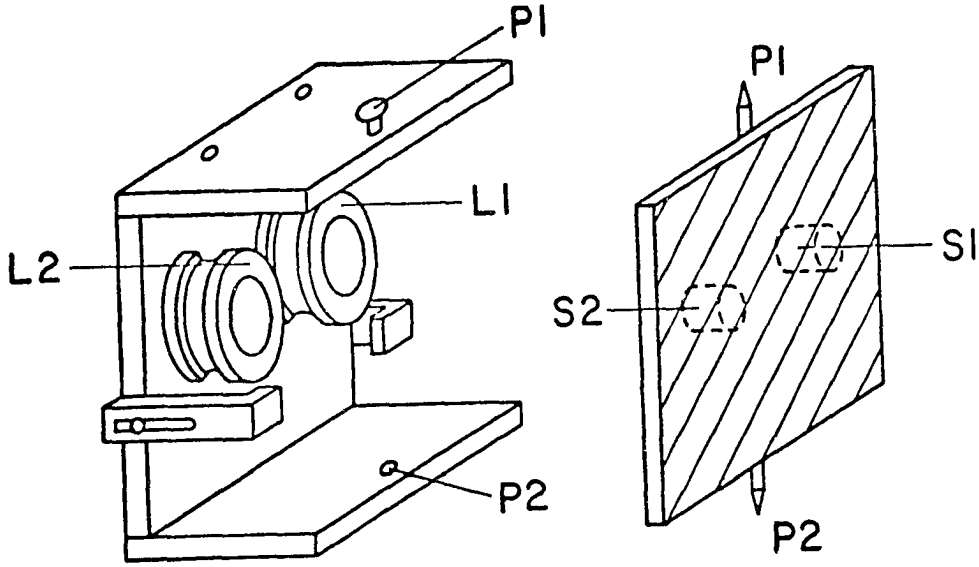

Figure 13: Schematic diagram of the driven mirror assembly. The permanent magnets (S1 and S2) attached to the back of the front surface mirror extend into the solenoids (L1 and L2). P1 and P2 are the pivot points

AC calorimeter electronics

A block diagram of the electronics used in the AC calorimeter is shown in Figure 14. The bias current for the bolometer is provided by mercury batteries. Adjustment is possible through a resistive voltage divider composed of metal film components. The bolometer and load resistor are maintained at liquid helium temperature. The signal ground was also established at the cold finger. The cryostat was the common ground point for all devices. It, in turn, was grounded to a cold water pipe.

The signal from the bolometer was fed into the input channels of both Ithaco 353 Lock-in Amplifiers. The reference signals for the lock-ins are derived from the chopper and mirror circuits as described above. The lock-in which detects at the chopper frequency is in the sum channel since the signal at this frequency is proportional to the sum of the absorptivities of the Ag reference film and the alloy sample. The lock-in tuned to the mirror frequency is in the difference channel since the signal is proportional to the difference in absorptivities.

The output from each lock-in amplifier is fed to a 1:10 voltage divider and then to a HP 2212A voltage to frequency converter (VFC). The two VFC outputs are input to a CMS 602A Electronic Counter which operates in the ratio mode. The counter readout is, therefore, equal to the ratio of the lock-in outputs. When the scales of the lock-in amplifiers are taken into account, this output is proportional to

$$(A_{alloy} - A_{pure})/(A_{alloy}+A_{pure}).$$

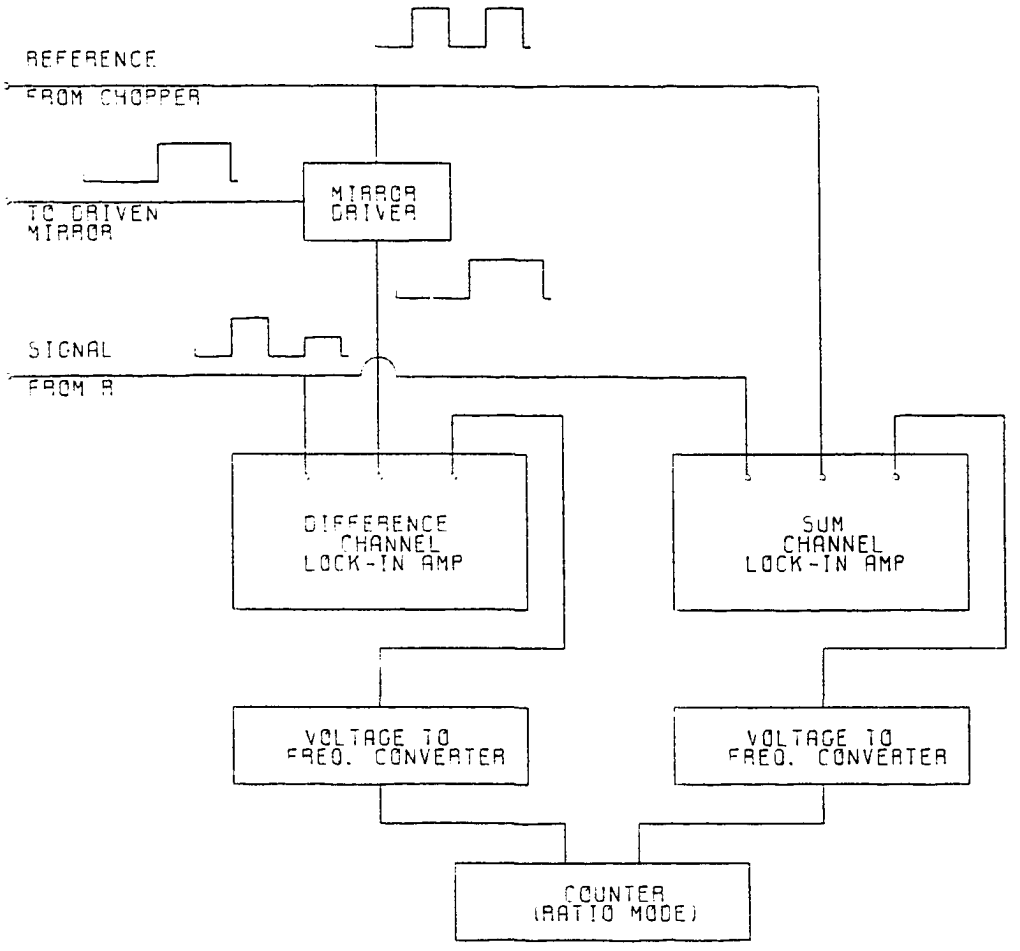

Figure 14: Block diagram of the electronics used in the AC calorimeter

Experimental procedures

In this section, the procedures followed in data acquisition are described. Emphasis is placed on the critical elements of the procedures.

Tuning the system involves setting final bolometer operating point, checking the optical alignment, adjusting the phase between the chopper and mirror driver and adjusting the phase of each lock-in amplifier for maximum output at the respective operating frequencies. A load curve was run prior to each of the final data sessions. This permitted proper choice of the bias current. The phase between the chopper and mirror was adjusted while monitoring the amplified waveform in the sum channel lock-in on an oscilloscope. The waveform is very sensitive to improper setting of this phase.

In the actual data acquisition phase, the most important procedure is maintaining a constant average power absorbed by the sample-bolometer system. Because of the sensitivity of the characteristics of the bolometer to the effective operating temperature, the sum channel output must be maintained at a constant value throughout the spectrum. This assures that the bolometer responsivity is constant for all data points.

The values reported in the next section are the average of three readings of the frequency counter. The counter, in effect, integrated the lock-in outputs over a 20 second time interval for each measurement.

RESULTS AND DISCUSSION

In this section, experimental spectra taken on the highest concentration sample are presented. The observed structure is discussed and compared with the observations of Koike, Yamaguchi and Hanyu. Finally, alternate explanations of the observed structure are explored.

Experimental results

Figure 15 shows the experimental spectrum for 0.75 atomic percent Ni in Ag over the energy range 0.3 to 3.3 eV. Two structure elements are apparent: a broad structure in the energy range 2.0 to 3.2 eV, and the general decline in $\Delta A/A$ from 0.3 to 0.5 eV. The most notable feature of the spectrum is the absence of structure in the 0.5 to 2.0 eV range where Koike *et al.*, report a VBS peak in Ag(Ni).

Other experimental spectra on another sample were taken as well. Sputtering targets, rates, environmental conditions and all other aspects of the experimental situation were nominally the same. This spectrum, taken over the energy range 0.62 to 3.5 eV, is consistent with the data shown in Figure 15. The predominant features are the broad structure above 2.0 eV and the absence of structure between 0.5 and 2.0 eV. The magnitude of the observed $\Delta A/A$ is significantly larger in this case, but the structural features are identical.

The observation that the magnitudes of $\Delta A/A$ are not reproducible between samples leads us to consider other mechanisms that may produce such differences. It is not surprising for optical measurements of metals in the region where they are highly reflective to differ in

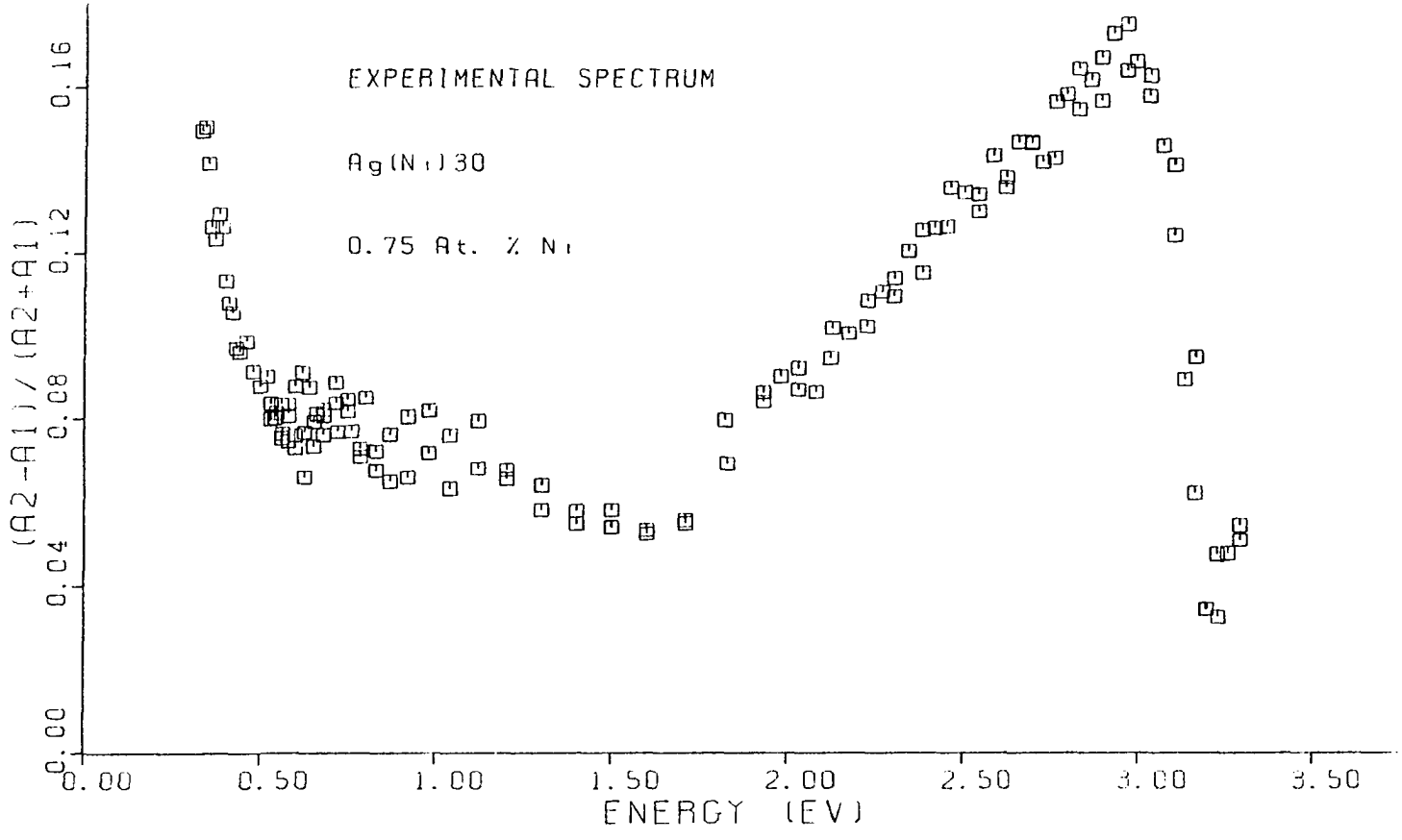

Figure 15: Differential absorptivity of Ag(Ni) from 0.3 to 3.3 eV

magnitude. Oxide formation is a common problem. Surface characteristics, such as roughness and grain boundaries, are also known to result in measurable differences in the observed optical properties of metals, especially below the plasma frequency. Before proceeding with analysis of these data for VBS structure, we examine our results for evidence of surface and structural effects.

Surface roughness effects

Surface roughness has been cited as a major contributor to measured dielectric properties in metals and semiconductors. While some measurement techniques are more sensitive than others to roughness, frequency dependent effects of surface roughness have been of interest to researchers whenever small effects are important. This is certainly the case in optical measurements in the free electron region of metals.

Aspnes, Theeten and Hottier [32] restrict themselves to situations where surface roughness is microscopic such that mean height and correlation length of irregularities are both much less than the wavelength of the light. They demonstrate that the effective medium approximation can be used to model surface roughness effects both in the Drude and interband regions of a metallic spectrum. Their approach requires building model surfaces composed of layers of effective media, each of which is composed of some combination of an oxide with voids or the pure substance with voids, sitting on the bulk material without voids. After demonstrating the ability of their approach to model observed spectra in Si, they examine topographical models of pure Si which would produce equivalent effects. Hemispherical or hemicylindrical

bosses and pits are determined to most closely reproduce their results. They find this encouraging, since it blends well with our understanding of the nucleation and growth of films.

Surface roughness effects have also been modeled by Beaglehole and Hunderi [33] assuming that the plane of the ideal surface is marred by randomly distributed hemispherical pits and bosses with optical properties differing from the bulk material. The observed change in reflectivity is calculated assuming both scattering and dipole absorption from these hemispherical defects. Part of the observed change in reflectivity can be explained by the diffuse scattering from the surface imperfections. However, they also observe changes in transmission that indicate absorption due to surface effects.

In an attempt to overcome the problem of restricted applicability when approximations are used, Hunderi and Beaglehole [34] chose a model for surface reflectivity which could be solved exactly. They considered a smooth surface with spheres of the same material located above it. Figure 16 shows a plot of $\Delta A/A$ calculated for Ag using this model. The calculation assumes that both reference and experimental films are silver, with the only difference being their roughness parameters. The parameters of the model are sphere size and fraction of the surface covered by the spheres. The difference in the absorption due to the structure shows a peak near 2.3 eV. Examination of the experimental spectrum in Figure 15 indicates that, if there is a structure due to surface roughness, it is buried in the low energy tail of the high energy

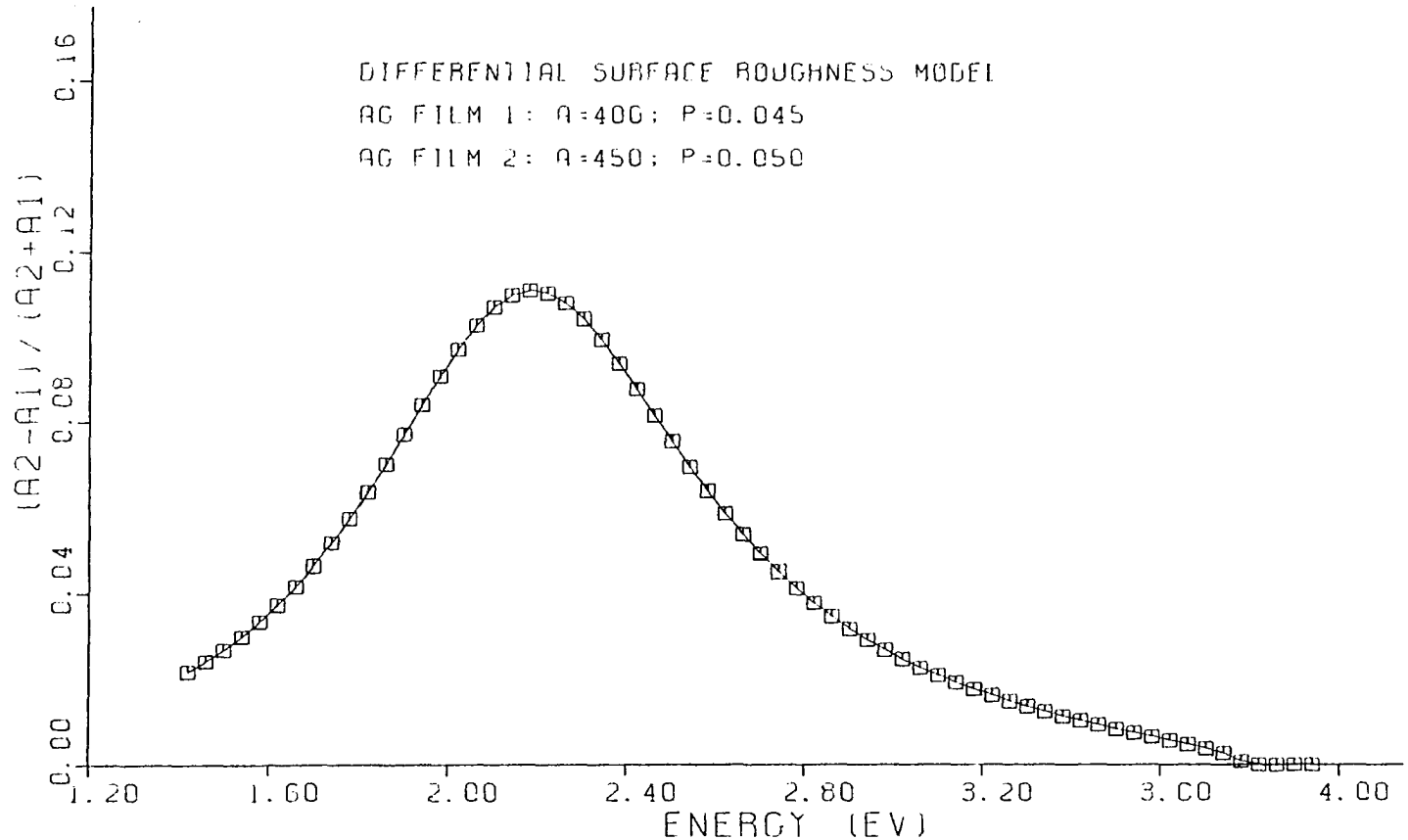

Figure 16: Model differential absorptivity of Ag films generated from the surface roughness model of Hunderi and Beaglehole [34]

peak. Clearly, surface roughness alone is not able to explain the observed spectra.

Grain boundary effects

Films deposited on substrates by either evaporation or sputtering are not single crystals. The samples are composed of arrays of grains which are oriented randomly. For isotropic materials, such as silver, the optical properties of the bulk silver away from the grain boundary will be the same for all grain orientations. However, within the grain boundaries themselves the crystal structure differs from that of the bulk and changes in optical properties can be expected. A differential technique such as the one used in this study can be expected to detect differences in grain boundary effects between the sample and reference films along with differences in the bulk properties of the sample and reference.

In a study of sample effects in Au films, Aspnes, Kinsbron and Bacon [35] concluded that the values of ε_2 in the Drude region are effected primarily by grain size in unannealed samples. They applied the effective medium approximation successfully to explain observed changes in $\tilde{\varepsilon}$ in the interband region. However, in the Drude region they note that ε_1 decreases in regions dominated by voids through the dependence of the plasma frequency on electron density. Their analysis of this region suggests that surface roughness may contribute to the masking of the threshold for interband transitions in Au when the samples are well annealed. Otherwise, it is not the dominant effect.

Nagel and Schnatterly [36] approached the problem of grain boundaries in films by assuming a two carrier model: electrons in the bulk and electrons in grain boundaries. The approach results in an expression that matches the form of experimentally determined frequency dependence of the relaxation time ($a + b\omega^2$). Their approximate result assumes that local field corrections are unimportant and that the optical mass of the two carriers are equal. The local field assumption is good as long as the frequency of the applied field is well below the plasma frequency. This assumption may not be good for the region of silver examined in this study, since the screened plasma frequency is 3.78 eV and measurements are made slightly above 3 eV.

Hunderi [37] developed a model which predicts the changes in optical properties of free electron metals due to the presence of grain boundaries and lattice defects and accounting for local field corrections. Figure 17 shows the grain structure of a typical thin film sample and a possible lattice structure near a grain boundary. The possible lattice structure clearly illustrates that the conduction electron density within the grain boundary can be expected to be different from that of the bulk material. The plasma frequency of the grain boundary material will be different from that of the bulk, and so will the optical properties.

Hunderi points out that the conduction electron density of the grain boundary material can be either greater or less than that of the bulk depending on the orientation of the two grains that meet at the boundary. The variation of the resulting plasma frequency between grains was

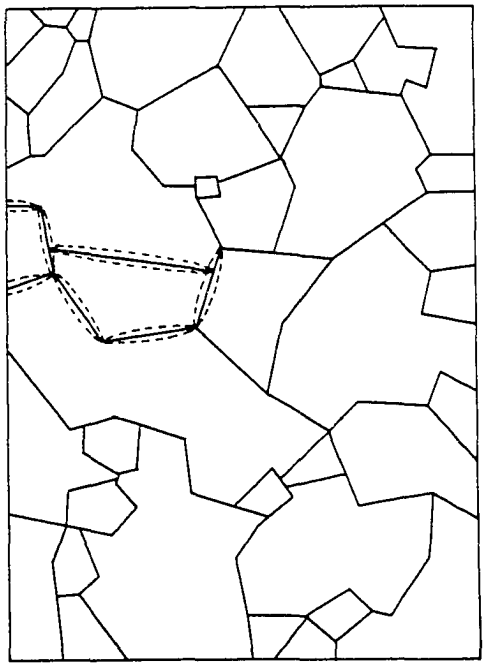

(a) Grain structure.

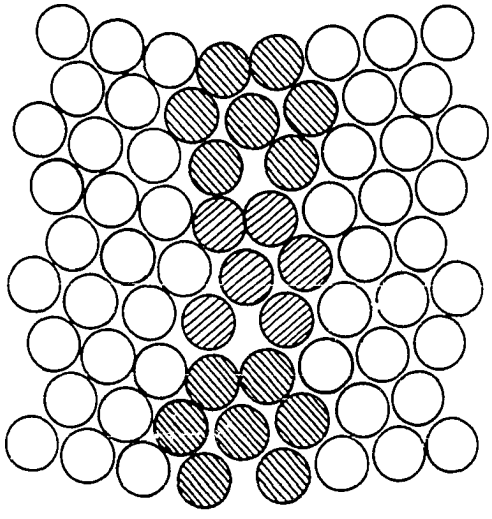

(b) Lattice structure.

Figure 17: Grain structure of a typical film and schematic diagram of lattice structure near a grain boundary. (a) Grain structure. The dashed lines show the ellipsoids where electron density differs from that of the bulk. (b) Lattice structure. The shaded circles represent atoms in the vicinity of a grain boundary. Reproduced from Hunderi [37]

assumed to follow a Gaussian distribution centered on the plasma frequency of the bulk.

The grain boundaries themselves were assumed to be ellipsoids (see the dotted line areas in Figure 17a). Non-spherical particles, even with an isotropic dielectric constant, exhibit polarization dependent scattering. The electrostatic polarizability of the particle, α_i, along an axis of the ellipsoid is given by

$$\alpha_i = \frac{V}{4\pi} \frac{\tilde{\varepsilon}_a - \tilde{\varepsilon}}{\tilde{\varepsilon} + (\tilde{\varepsilon}_a - \tilde{e})L_i} \tag{59}$$

where V is the volume of the ellipsoid, $\tilde{\varepsilon}$ is the dielectric constant of the medium surrounding the ellipsoid, $\tilde{\varepsilon}_a$ is the dielectric constant of the ellipsoid, and L_i is the depolarization factor along the i^{th} axis of the ellipsoid. Assuming that one major axis of the ellipsoid is always oriented normal to the surface of the sample, Hunderi derived an expression for the reflectivity of the sample due to the presence of a set of equivalent ellipsoids:

$$R = R_0 \left| \frac{1 - V_f \alpha_f [(1+\tilde{N})/(1-\tilde{N})]}{1 - V_f \alpha_f [(1-\tilde{N})/(1+\tilde{N})]} \right|^2 \tag{60}$$

where $\tilde{N}$ is the complex index of refraction of the ellipsoid material, and V_f is the volume fraction of sample occupied by ellipsoids of that type. When more than one type of particle is present, the term $V_f \alpha_f$ is replaced by a sum $V_f \sum_i g_f^i \alpha_f^i$. V_f is the fractional volume occupied by all ellipsoids, g_f^i is the fraction of ellipsoids of type i, and α_f^i is the polarizability of particles of type i.

Figure 18 shows $\Delta A/(A_1 + A_2)$ calculated assuming the bulk material for both reference and sample to be silver. Ellipsoids of grain boundary material are assumed to have equal depolarization factors. The effect of changing both V_f and σ, the width of the distribution of plasma frequencies ($\sigma = \omega_p/DIV$), is apparent. The notable features of this figure are that a peak is exhibited at approximately 3.0 eV in all cases and that the principal difference between the calculated quantities lies in the low energy tail. The position of this peak closely matches that observed in the experimental spectrum (Figure 15).

The similarities observed between the observed and calculated $\Delta A/(A_1 + A_2)$ suggest an attempt to fit the observed spectrum to a calculated spectrum. The spectral features that can be explained by this structural difference in the two films can be eliminated as candidates for evidence supporting the existence of virtual bound states in dilute Ag(Ni) alloys. Unfortunately, the quantity $\Delta A/(A_1 + A_2)$ is not readily reduced to a quantity that is able to be compared directly with a theoretical model of the dielectric function for a material. Such a reduction would be possible only if it were reasonable to assume that A_1 and A_2 were approximately equal. The experimental data show that the sample and reference absorptivities differ by as much as 30% in the energy range near 3.0 eV. This situation dictates a less direct test of the assumption that observed structure is due to differences in grain boundary structure or density.

The model assumed for comparison with the experimental data is a situation physically identical to that used in this study: two films

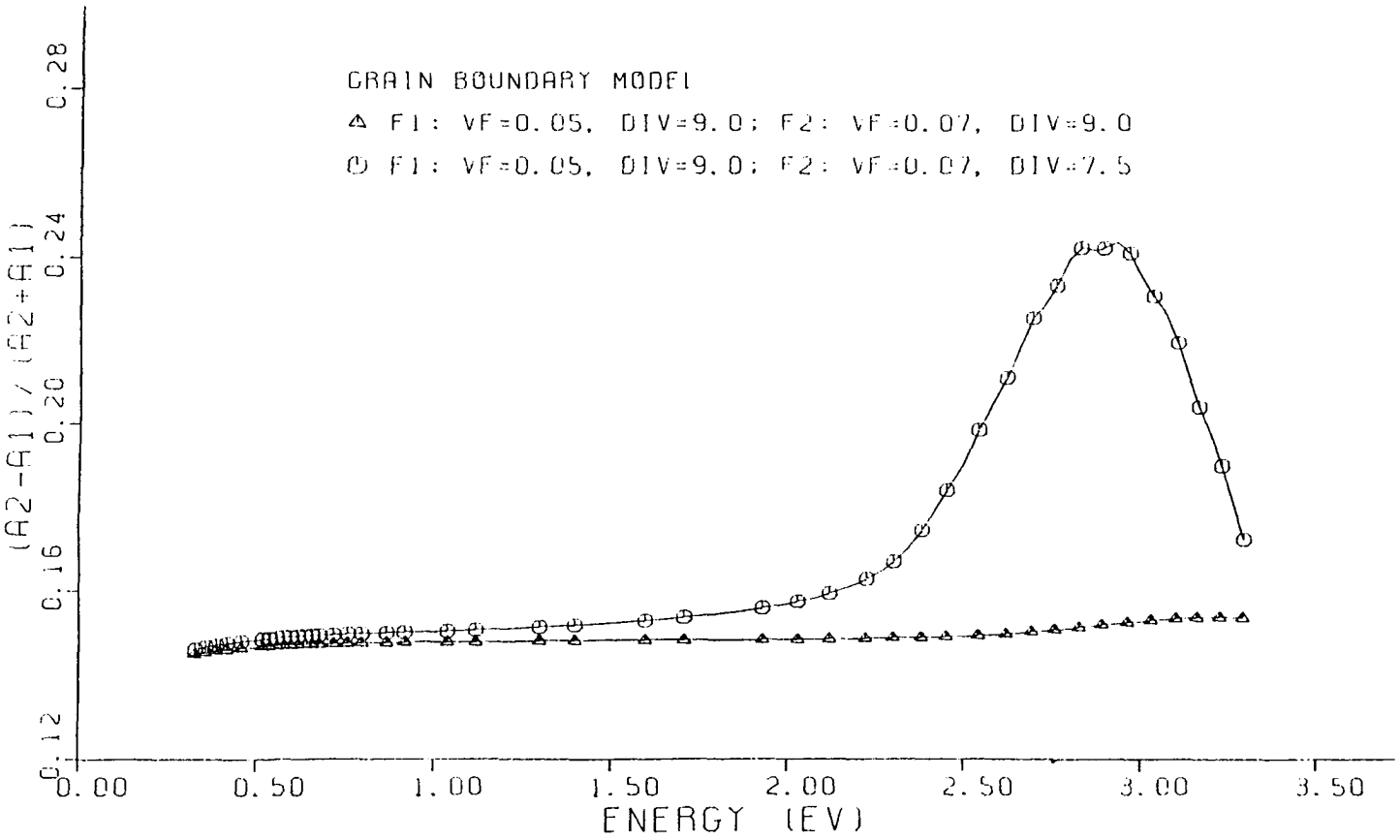

Figure 18: Model differential absorptivity of Ag films using the formulation of Hunderi. In one case, the reference film (F1) differs from the sample film (F2) only in the volume fraction of grain boundary material (VF). In the second case, both volume fraction (VF) and width of the distribution of plasma frequencies (DIV) are changed

deposited on a single substrate at different times. The important difference is that this model assumes both films to be pure silver. Because the two films were deposited at different times, we assume that there are differences in the grain structures of the two films that lead to the observed differences in absorptivity. The model is not able to distinguish between mechanisms which produce different grain sizes. Therefore, if Ni in Ag causes the grain size of the sample to change from the pure Ag situation without altering the absorptivity of the bulk regions of the sample, the model is incapable of distinguishing this case from two pure Ag films with distinct grain structures due to deposition differences.

Hunderi's model of reflectivity in the presence of grain boundaries was assumed to apply to both the reference and sample sides of the substrate. The absorptivity of each side was calculated ($A = 1 - R$ in an opaque sample). Ellipsoid shape was assumed to be identical for all grain boundaries, resulting in identical depolarization factors for all grain boundaries. The orientation of the grain boundaries is assumed to be distributed randomly, resulting in a distribution of effective plasma frequencies within the boundary material. Finally, the volume fraction of grain boundary material present in the regions where absorptivity was measured is assumed to be different. When the absorptivity of the two model films is calculated, the quantity $\Delta A/(A_1 + A_2)$ for the combination is computed. The resulting spectrum is compared with the observed spectrum.

Since the procedure used does not yield a readily derivable functional form for the quantity $\Delta A/(A_1 + A_2)$, a formal least squares fitting procedure is not appropriate. Instead, at the end of each model calculation the spectral distribution of the calculated $\Delta A/(A_1 + A_2)$ is compared with the measured quantity. The sum of squares of the deviations of the experimental data points from the corresponding model values was computed. The sum of squares was minimized by systematically changing the quantities V_f and D. No measure of statistical significance is available in this procedure.

The quantity V_f was varied first in order to obtain the best fit in the low energy range of the spectrum, $E \leq 1.0$ eV. When the sum of squares was minimimized by the choice of an appropriate V_f, the widths of the distribution of plasma frequencies in the grain boundary materials of the reference and sample were varied to obtain the best fit to the peak height and position. For this latter case, the sum of squares was computed for the entire available energy range. Figure 19 shows the result of this fitting procedure.

The best fit between the model and experimental data resulted in a sum of squares of 0.02929.

The parameters of the model which resulted in this surprisingly good fit are summarized in Table 2. The quantity D is a measure of the width of the distribution of plasma frequencies in the grain boundary material. In the model calculation, the standard deviation of distribution is computed by dividing the plasma frequency of bulk silver by the quantity D. This implies that a lower value of D represents a more broadly

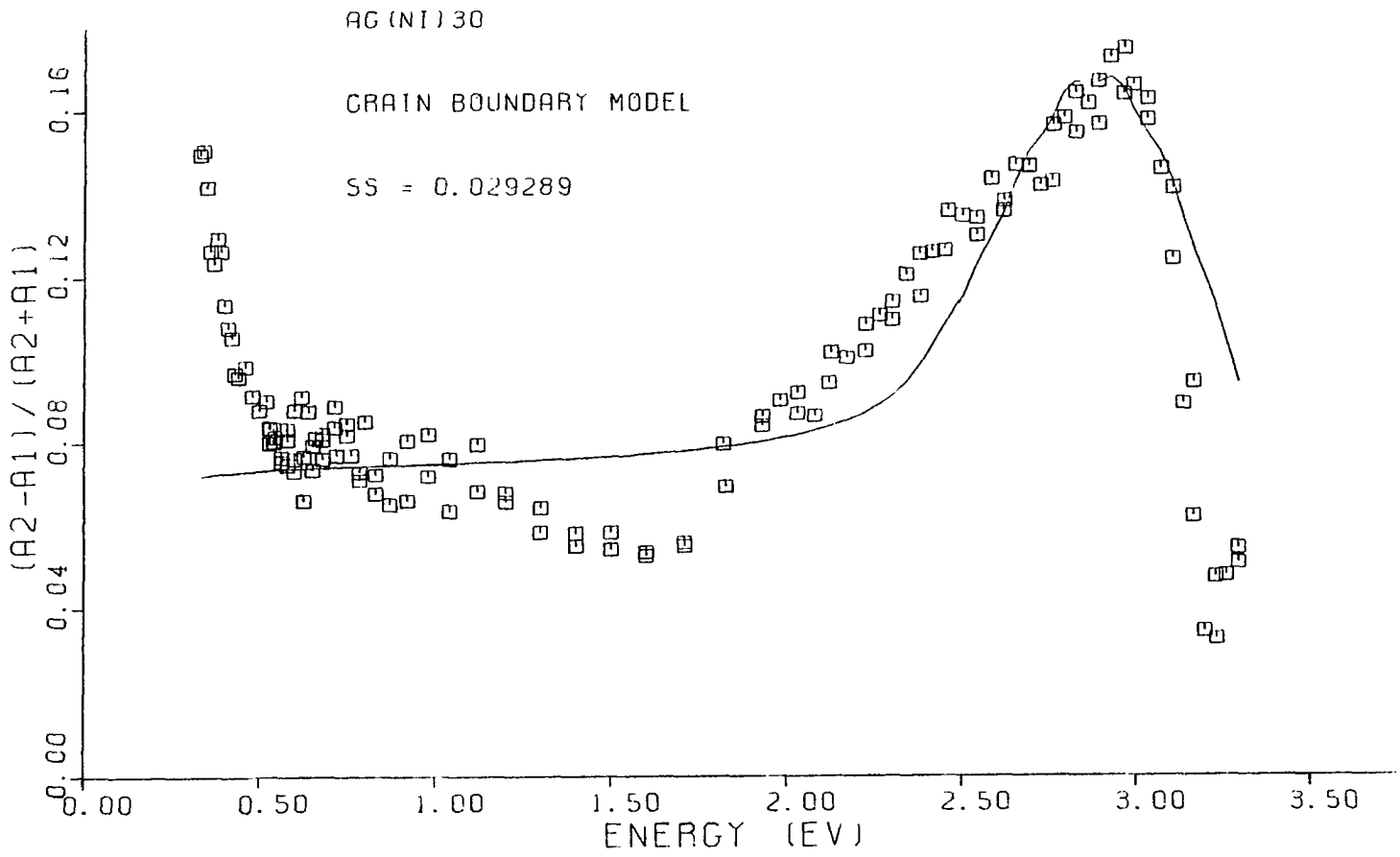

Figure 19: Best fit between experimental data and grain boundary model of Hunderi. The solid line is the calculated differential absorptivity. The discrete points are the experimental data

distributed range of effective plasma frequencies in the grain boundaries. The parameters L_1 and L_2 were chosen for consistency with the calculations of Hunderi. They are characteristic of samples with grain diameters > 0.2 microns. The quantity V_f is the assumed volume fraction occupied by grain boundary material.

Table 2: Grain Boundary Model Parameters in Successful Fit with Observed Ag(Ni) Spectrum

Parameter	Reference	Sample
D	9.0	7.5
L_1	0.8	0.8
L_2	0.0	0.0
V_f	0.050	0.059

From this model calculation and fit with experimental data, it is apparent that the high energy structure in the spectrum can be explained by grain boundary and lattice defect differences between the reference and experimental samples. It should not be attributed to a virtual bound state in Ag(Ni).

Low energy structure

The low energy structure apparent in Figure 16 is not characteristic of either surface roughness or grain boundary effects. Unfortunately, the data to not extend to low enough energy to locate the position of a peak. One additional phenomenon is known to contribute to structure in

optical spectra in this energy range. The anomolous skin effect (ASE) is a well established source of additional absorption in metals in the infrared. Examination of the likelihood of ASE structure is appropriate.

In the infrared, highly reflective metals can also exhibit optical absorption due to non-local effects. Kliewer and Fuchs [38] have developed a model of the anomolous skin effect that explains some of these deviations from normal free electron-like behavior. Using their formulation for absorption at normal incidence and estimating the dc conductivity at 4.2 K required in their equations by assuming that sample and reference films had different resistivity ratios, the ASE absorption of each film was calculated over the range 0.1 - 1.5 eV. A silver film with a resistivity ratio of 10 has ASE absorptivity ranging from 0.0046 to 0.0047 over the range. A silver film with a resistivity ratio of 15 had ASE absorptivity ranging from 0.00418 to 0.00425. These two films would yield value of $(A_2-A_1)/(A_2+A_1)$ which increased monotonically from 0.045 to 0.048 over the range. The anomolous skin effect is not large enough to explain the low energy structure. The low energy structure does not seem to be due to non-local effects.

Comparison with other research

The low energy structure observed in Figure 15 is not due to roughness, grain boundaries or non-local effects. We now examine these data in light of that of other researchers under the assumption that the structure is due to the difference between Ag and Ag(Ni) alloy.

As noted earlier, Koike, Yamaguchi and Hanyu [26] observed two structures in their spectra of Ag(Ni) alloys, one at 0.5 and one at 1.8

eV. They note that the d-states of Ni in noble metals are not expected to split and recall that no splitting is observed in either Cu(Ni) or Au(Ni). One of the peaks must be eliminated as a candidate for the VBS peak in Ag(Ni).

Figure 20 reproduces their plot of impurity resistivity data. They display data from other studies on impurity resistivity of transition metals in Cu and Au along with their measurements of transition metals in Ag. Impurity resistivity is a function of free carrier concentration (N) and the probability of scattering ($1/\tau_{imp}$). Little change in resistivity upon alloying implies that the density of states at the Fermi energy is changed very little and that there are few localized impurity states at the Fermi energy. The measurement for Ag(Ni) indicates that only the tail of a VBS distribution may persist to the Fermi energy. Using the positions, E_d, determined from the locations of the structures at 0.5 and 1.8 eV, they calculate Δ for VBS peaks such that the observed impurity resistivity is matched. They obtain 0.17 and 0.6 eV, respectively.

In order to select the appropriate structure as a VBS structure, they consider systematics of the other transition metals in Ag and of Ni in Cu and Au. Their computed Δ for the VBS peak in AgTi is 0.4 eV. By comparison, they suggest that 0.17 eV is too small for Ag(Ni). They also recall data on Pd in Cu, Ag, and Au to suggest that E_d tends to be further from the Fermi energy in Cu and Ag and that Δ tends to be broader in Ag hosts than in either Cu or Au. Unfortunately, the data cited for CuPd are reflectivity data taken on fairly high concentration alloys [19], the reported structure overlaps the onset of interband transitions

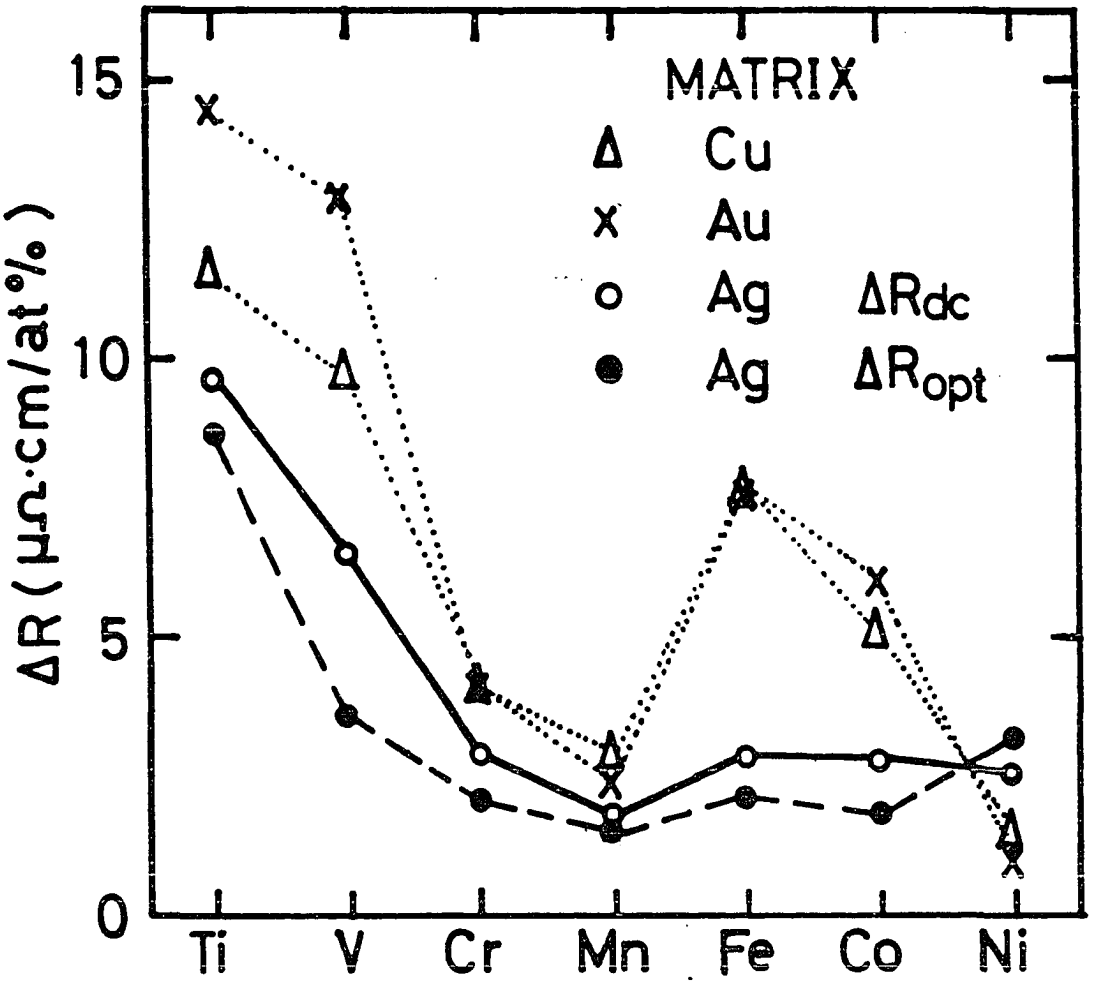

Figure 20: Impurity resistivity of Ag-based transition metal alloys at room temperature. The solid line is the dc resistivity and the dashed line shows the impurity resistivity calculated from optical data. The data for the Cu- and Au-matrix are shown by dotted lines. Reproduced from Koike, Yamaguchi, and Hanyu [26]

in Cu, and no estimate of Δ is possible from the data. Citing the well established VBS parameters of Cu(Ni) and Au(Ni), they then assign the higher energy structure as a VBS structure.

In a later paper, Koike [39] reports the thermoelectric power (TEP) of the Ag-based transition metal alloys. Thermoelectric power, like resistivity, is a quantity associated with the Fermi surface. It is proportional to the slope of the density of states at the Fermi level. Figure 21, taken from their paper, also contains TEP data on transition metals in Cu and Au. Their measurement places the TEP of Ag(Ni) slightly above Cu(Ni) but well below Au(Ni). The calculation of TEP from E_d and Δ determined from their optical measurements yields a value approximately 1/3 of the measured value and less than 1/2 of the measured TEP for Cu(Ni). The choice of $E_d = 0.5$ and $\Delta = 0.17$ eV would yield a TEP value 3.5 times their calculated value, a much closer agreement with experiment.

The systematics presented by Koike, Yamaguchi and Hanyu do not seem to support their choice of E_d and Δ as convincingly when the TEP data are taken into account. Figure 22 graphically presents the Ni and Pd data they cite. In the figure, the position of E_d is marked by a horizontal line and the length of the vertical line is 2Δ centered about E_d for experimentally determined VBS states. Two entries for Ag(Ni) are indicated by o's at the proposed locations of E_d the proposed values for Δ are indicated in the same manner as the more positively assigned structures.

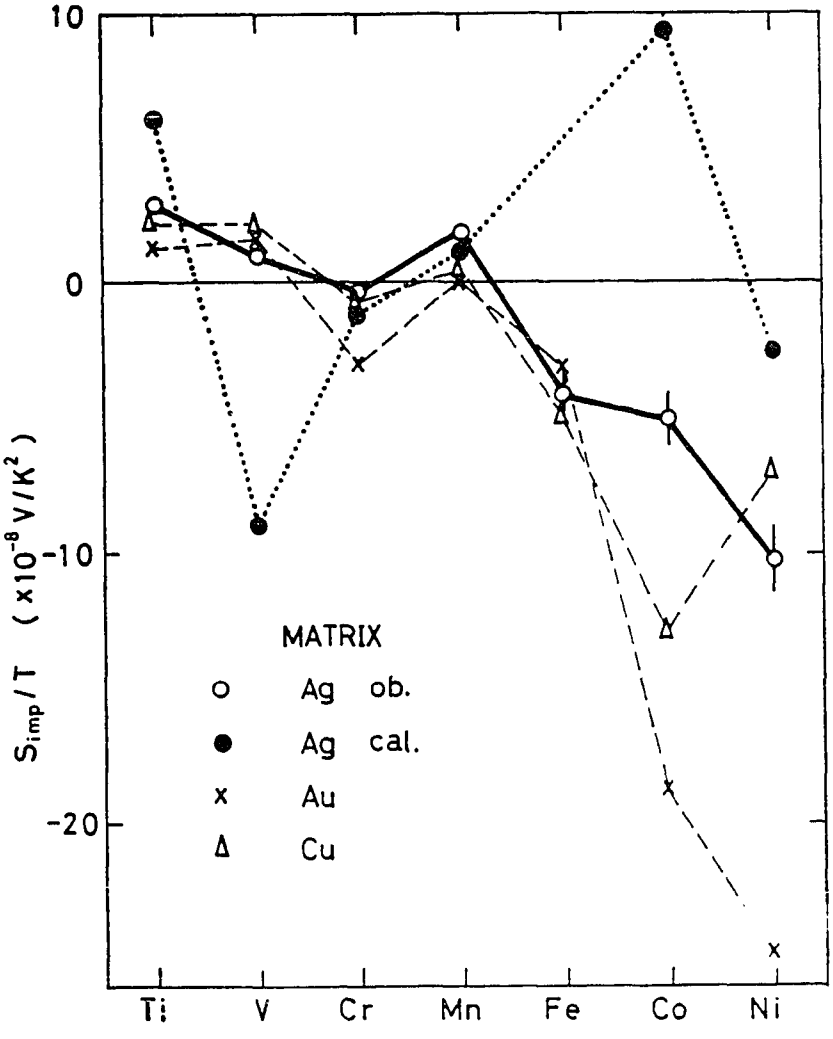

Figure 21: Impurity thermoelectric power as a function of solute metal at room temperature: solid line, S_{imp} for Ag-based alloys; dotted line, S_{imp} calculated using the VBS parameters of Koike, Yamaguchi, and Hanyu [26] for Ag-based alloys; dashed lines, S_{imp} for Au- and Cu-based alloys. Reproduced from Koike [39]

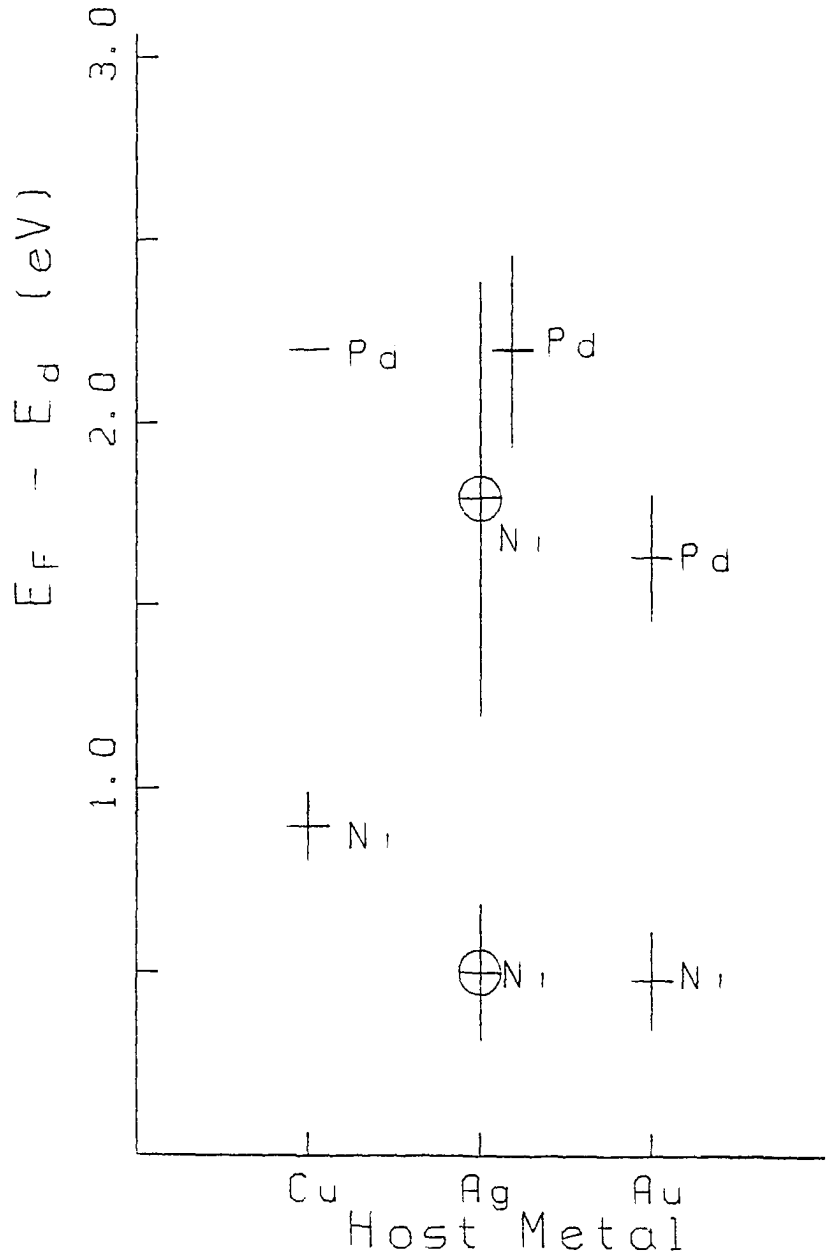

Figure 22: Virtual bound state parameters for Ni and Pd in the noble metals. The two sets of parameters for Ni in Ag are for the two structures observed by Koike, Yamaguchi, and Hanyu

Even if we accept the tentative assignment of a VBS state in Cu(Pd) centered somewhat above 2.2 eV, the systematics seem to favor Ag-hosted alloys as having VBS states positioned between the states in Cu- and Au-based alloys with the same transition metal. The value of Δ does seem to be slightly larger in Cu and Ag than in Au. The choice of the lower structure as a VBS state seems to be more consistent with the patterns than Koike, Yamaguchi and Hanyu's choice.

The resistivity data indicate that there is little difference in the density of impurity states at the Fermi energy. A slightly greater density of impurity states than their choice provides for Ag(Ni) would result in the slightly higher observed impurity resistivity. The similarity in the impurity resistivities is more striking than the differences.

The TEP experimental data for the three hosts also seem to favor less variation in VBS position and shape than proposed by Koike, Yamaguchi and Hanyu. Figure 23 sketches VBS position and shape possibilities that seem more consistent with the optical, resistivity and TEP data and with the systematics discussed above. As the figure shows, the density of impurity states should be nearly the same in all three hosts. The width of the localized states is broader in Cu and Ag and the slope of the impurity density of states at the Fermi energy is steeper in Au than in either Cu or Ag. Considering the absence of structure at 1.8 eV in these measurements and all of the data of Koike, Yamaguchi and Hanyu with that of Koike, the 0.5 eV structure seems to be the more likely candidate for the VBS peak.

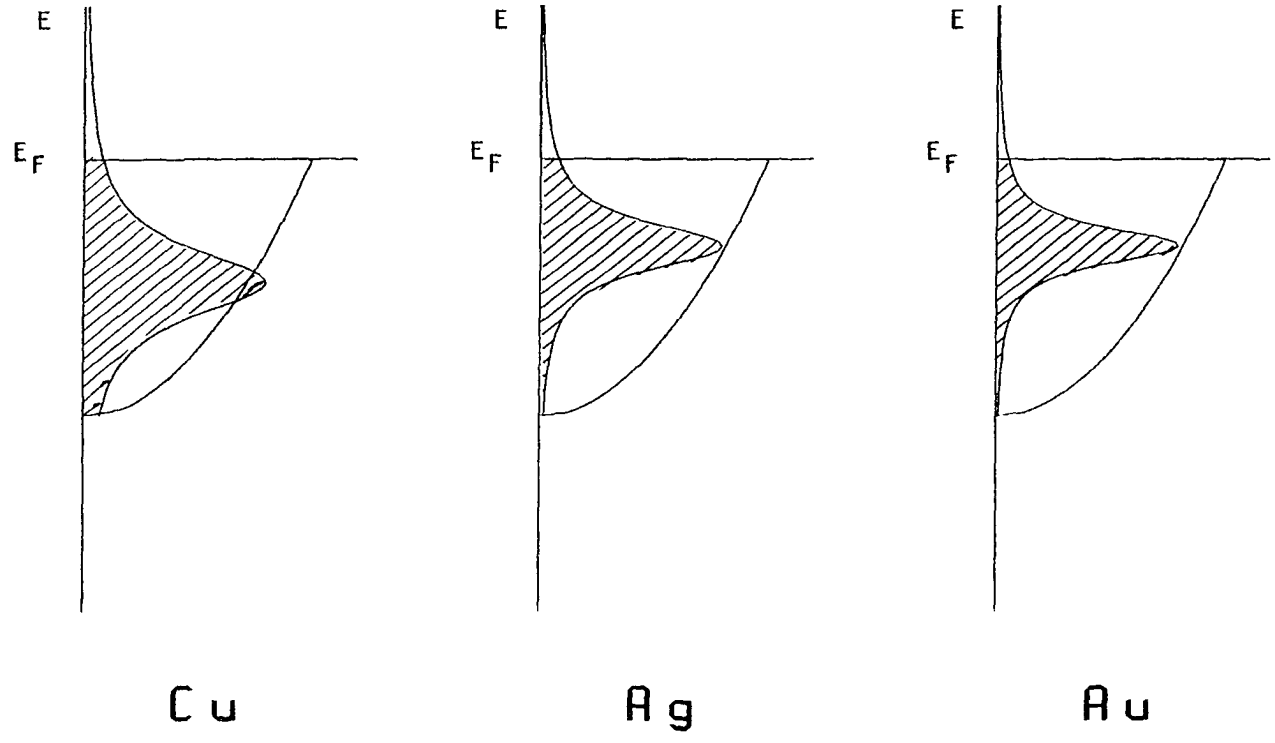

Figure 23: Schematic representation of the virtual bound state density of states of Ni in the noble metals. The shaded areas are the filled portion of the VBS band. E_F is the Fermi energy

It is tempting to examine the systematics of d-band position in the pure transition metals to confirm the assignments made above. However, the assignment of d-band position across the transition metals is not known with confidence. In general, if we assumed that d-bands have a constant width across the transition metal series, we would expect the occupied portion of the band to increase as we move to higher Z metals. Virtual bound states for the low Z transition metals would lie in the unoccupied portion of the band. Toward the middle of the series, VBS structure would move toward the Fermi energy, resulting in low energy optical structure. On the high Z end of the series, we would expect VBS states to emerge in the occupied portion of the bands. The d-band to Fermi surface transitions in Cu would be a plausible limit to the VBS positions in occupied regions of the energy bands since they represent a full band, expected to be most tightly bound to the core. Optical structure associated with VBS transitions would be expected to be higher in energy at either end of the transition metal series than in the middle

The real situation in transition metals is complicated by exchange splitting in the middle of the series. Band calculations of the ferromagnetic transition metals show that the splitting can be as much as 2 eV. The complication in band structure and the accompanying increase in optical transition possibilities throughout the Brillouin zone has made it difficult to identify structure in optical spectra and therefore difficult to assign structure to transitions.

The fact that there is significant exchange splitting is clear and at least one system (Ag(Mn)) has been identified which shows both an

occupied and an unoccupied VBS state. In such systems E_d is expected to be farther removed from the Fermi energy and the density of impurity states at the Fermi level should be lower than expected for unsplit cases. Impurity contributions to resistivity and to TEP would be expected to be at a minimum in the middle of the transition metal series as a result.

The systematics of the transition metals as described seem to work fairly well in the first half of the 3d transition metal series. However, the simplified explanation seems to fall apart in the high Z end.

The fact that the low energy structure is observed both in this study and in Koike, Yamaguchi and Hanyu's study while their high energy structure is not observed in this study makes it important to reconsider their assignment of VBS parameters. We have demonstrated that the choice of the low energy structure as a VBS peak is more consistent with all their data and consistent with the systematics of the best established transition metals in noble metal hosts.

Despite the above arguments, the identification of a VBS centered at 0.5 eV in Ag(Ni) is far from conclusive. Unfortunately, Koike, Yamaguchi and Hanyu's data show similar low energy structure in other alloys and they do not always treat it with equal seriousness. In many cases, their data, like those in this study, do not extend to low enough energy for the peak maximum to be directly measured. They infer the existence of a peak by extrapolating their data to the zero frequency value. The VBS position assignments for Ag(Ti) and Ag(Co) fall in the extrapolated

region. Similar structure is present in spectra of Ag(V), Ag(Mn) and Ag(Fe), yet no low energy VBS states are identified in these systems. The low energy portion of their data seems to be suspect.

The low energy data in this study are more certain. The detector's characteristics did not vary across the measured range. Maintaining a constant average power absorbed insured that the detector was always operating at the same point on its load curve. Spectral variation in detector sensitivity is not a factor. The low energy structure is real, albeit incompletely measured.

Until very recently, no calculation of the electronic structure of Ag(Ni) has been available. Singh, Raj and Prakash [40] have reported calculations on Cu(Ni) and Ag(Ni) using their pseudo-Green's function formalism. Their results yield E_d and Δ of 0.74 and 0.23 eV for Cu(Ni) and 0.68 and 0.33 eV for Ag(Ni). Their prediction of VBS structure for Ni in Ag host at lower energy than in the Cu host is consistent with the measurements and tentative assignments made in this study.

Conclusions

Despite the encouraging agreement between the VBS assignment made here and the calculations of Singh, Raj and Prakash, the results of this study are not able to unequivocably verify the existence or non-existence of a VBS in Ag(Ni). There are indications that a virtual bound state peak does exist, but at the lower of the two energies considered by Koike et al. These results call for measurements that extend lower in energy than what was achieved in this study. Measurements of optical absorptivity of Ag(Ni) that extend farther into the infrared would

resolve the question of whether or not the structure is really part of a peak and permit direct measurement of E_d and Δ.

REFERENCES

[1] H. Ehrenreich and M. H. Cohen, Phys. Rev. 115, 786 (1959).

[2] H. Ehrenreich and H. R. Philipp, Phys. Rev. 128, 1622 (1962).

[3] P. B. Johnson and R. W. Christy, Phys. Rev. B 6, 4370 (1972).

[4] J. Friedel, Nuovo Cim. Suppl. 7, 287 (1958).

[5] P. W. Anderson, Phys. Rev. 124, 41 (1961).

[6] D. J. Sellmyer, in Solid State Physics, Vol. 33, edited by H. Ehrenreich, F. Seitz and D. Turnbull (Academic Press, New York, 1978), p. 100.

[7] B. Caroli, Phys. Kondens. Materie. 1 346, (1963).

[8] B. Kjöllerström, Phil. Mag. 19, 1207 (1968).

[9] D. Beaglehole, J. Phys. F: Metal Phys. 5, 657 (1975).

[10] D. Beaglehole, Phys. Rev. B 14, 341 (1976).

[11] G. M. Stocks, R. W. Williams and J. S. Faulkner, Phys. Rev. 156, 1017 (1971).

[12] R. Reidinger, J. Phys. F: Metal Phys. 1, 392 (1971).

[13] C. L. Cook and P. V. Smith, J. Phys. F: Metal Phys. 4, 1344 (1974).

[14] M. Bassett and D. Beaglehole, J. Phys. F: Metal Phys. 6, 1211 (1976).

[15] F. Abeles, J. de Physique et le Radium. 23, 677 (1962).

[16] H. P. Myers, C. Norris, and L. Wallden, Solid State Commun. 7, 1539 (1969).

[17] J. Feinleib, W. J. Scouler and J. Hanus, J. Appl. Phys. 40, 1400 (1969).

[18] C. Norris, J. Appl. Phys. 40, 1396 (1969).

[19] L. E. Wallden, D. H. Seib and W. E. Spicer, J. Appl. Phys. 40, 1281 (1969).

[20] H. D. Drew and R. E. Doezema, Phys. Rev. Letters 28, 1581 (1972).

[21] D. Beaglehole and C. Kunz, J. Phys. F: Metal Phys. 7, 1923 (1977).

[22] B. Y. Lao, R. E. Doezema and H. D. Drew, Solid State Communications 15, 1253 (1974).

[23] A. B. Callender and S. E. Schnatterly, Phys. Rev. B 7, 4385 (1973).

[24] J. Lafait, C. R. Acad. Sci. (Paris) 279, B59 (1974).

[25] M. L. Theye, Thesis (University of Paris, 1968) (Unpublished).

[26] H. Koike, S. Yamaguchi and T. Hanyu, J. Phys. Soc. Jpn. 38, 1370 (1975).

[27] O. D. R. Hunderi, Ph. D. dissertation, U. of Maryland (1970).

[28] F. J. Low, J. Opt. Soc. Am. 51, 1300 (1961).

[29] R. Clark Jones, J. Opt. Soc. Am. 43, 1 (1953).

[30] S. Zwerdling, R. A. Smith and J. P. Theriault, Infrared Physics 8, 271 (1968).

[31] H. D. Drew, Ph. D. dissertation, Cornell Univ. (1968).

[32] D. E. Aspnes, J. B. Theeten, and F. Hottier, Phys. Rev. B 20, 3292 (1979).

[33] D. Beaglehole and O. Hunderi, Phys. Rev. B 2, 301 (1970).

[34] O. Hunderi and D. Beaglehole, Phys. Rev. B 2, 321 (1970).

[35] D. E. Aspnes, E. Kinsbron and D. D. Bacon, Phys. Rev. B 21, 3290 (1980).

[36] S. R. Nagel and S. E. Schnatterly, Phys. Rev. B 9, 1299 (1974).

[37] Ola Hunderi, Phys. Rev. B 7, 3419 (1973).

[38] K. L. Kliewer and Ronald Fuchs, Phys. Rev. B 2, 2923 (1970).

[39] Hideaki Koike, J. Phys. Soc. Japan 40, 737 (1976).

[40] J. Singh, S. D. Raj and S. Prakash, Nuovo Cimento D 4, 469 (1984).